

# Magnetic Shielding of the Acceleration Channel Walls in a Long-Life Hall Thruster

Ioannis G. Mikellides,<sup>\*</sup> Ira Katz,<sup>†</sup> Richard R. Hofer,<sup>‡</sup> Dan M. Goebel,<sup>§</sup>  
*Jet Propulsion Laboratory, California Institute of Technology, Pasadena, CA, 91109*

and

Kristi de Grys,<sup>\*\*</sup> Alex Mathers<sup>††</sup>  
*Aerojet, Redmond, WA 98052*

**In a Qualification Life Test (QLT) of the BPT-4000 Hall thruster that recently accumulated >10,000 h it was found that the erosion of the acceleration channel practically stopped after ~5,600 h. Numerical simulations of this thruster using a 2-D axisymmetric, magnetic field-aligned-mesh (MFAM) plasma solver reveal that the process that led to this significant reduction of the erosion was multifaceted. It is found that when the channel receded from its early-in-life geometry to its steady-state configuration several changes in the near-wall plasma and sheath were induced by the magnetic field that, collectively, constituted an effective shielding of the walls from any significant ion bombardment. Because all such changes in the behavior of the ionized gas near the eroding surfaces were caused by the topology of the magnetic field there, we term this process “magnetic shielding.”**

## Nomenclature

$A_{0,1,2}$  = fitting coefficients for electron excitation energy loss  
 $\mathbf{B}$  = magnetic induction field  
 $C_{0,1,2,3}$  = fitting coefficients for the H&W sheath  
 $c_{0,1,2,3}$  = fitting coefficients for  $f_{\theta(K)}$   
 $\mathbf{E}$  = electric field  
 $e$  = electron charge,  $1.602 \times 10^{-19}$  C  
 $\mathbf{\bar{I}}_i$  = inelastic ion drag force density  
 $I_b$  = total ion beam current  
 $I_i$  = ion species current  
 $f$  = neutral velocity distribution function  
 $f_{\theta(K)}$  = fitting functions for the angle (energy) dependence of the sputtering yield  
 $\mathbf{j}_e$  = electron current density  
 $\mathbf{j}_i$  = ion current density  
 $K_T$  = fitting coefficient for  $f_K$   
 $K_{e0}/2$  = first Maxwellian cross-over

$Q_e^T$  = thermal heating of electrons  
 $q_i$  = ion charge (eZ)  
 $p_{i(e)}$  = ion (electron) pressure, Pa

## Greek Symbols

$\alpha$  = spatially varying multiplier for  $v_\alpha$   
 $\hat{\mathbf{b}}$  = magnetic induction field unit vector  
 $\Delta A, \Delta V$  = computational area and volume increments  
 $\Delta\phi$  = sheath potential drop at channel walls  
 $\varepsilon$  = erosion rate  
 $\varepsilon_0$  = permittivity in vacuum  
 $\zeta_{es}$  = ionization potential of species “s”  
 $\eta$  = total or effective electrical resistivity  
 $\eta_b$  = current utilization efficiency  
 $\eta_{ei}$  = electron-ion electrical resistivity  
 $\eta_m$  = mass utilization efficiency  
 $\theta$  = ion incidence angle

<sup>\*</sup> Member of the Technical Staff, Electric Propulsion Group, 4800 Oak Grove Drive, Pasadena, CA, 91109, Mail Stop 125-109, Associate Fellow AIAA.

<sup>†</sup> Group Supervisor, Electric Propulsion Group, 4800 Oak Grove Drive, Pasadena, CA, 91109, Mail Stop 125-109, Senior Member AIAA.

<sup>‡</sup> Member of the Technical Staff, Electric Propulsion Group, 4800 Oak Grove Drive, Pasadena, CA, 91109, Mail Stop 125-109, Senior Member AIAA.

<sup>§</sup> Section Staff, Thermal and Propulsion Engineering Section, 4800 Oak Grove Drive, Pasadena, CA, 91109, Mail Stop 125-109, Associate Fellow AIAA.

<sup>\*\*</sup> Manager, Electric Propulsion Systems, P.O. Box 97009, Redmond, WA, 98073-9709, Member AIAA.

<sup>††</sup> Program Manager, Electric Propulsion Systems, P.O. Box 97009, Redmond, WA, 98073-9709, Member AIAA.

$K_i$ = ion kinetic energy	$\kappa_e$ = electron thermal conductivity
$k_B$ = Boltzmann's constant	$\Lambda_{i\beta}$ = coulomb logarithm for i- $\beta$ pair
$L$ = acceleration channel length at BOL	$\lambda_{mfp}$ = mean free path for (classical) collisions
$R$ = radius of acceleration channel centerline at BOL	$\nu_\alpha$ = non-classical collision frequency
$R_{i(e)}$ = elastic ion (electron) drag force density	$\nu_B$ = Bohm collision frequency
$S_e$ = secondary electron yield	$\nu_e$ = total collision frequency
$t$ = time	$\nu_{ei}$ = electron-ion (coulomb) collision frequency
$T_{i(e)(\beta)}$ = ion (electron) (ion species $\beta$ ) temperature	$\nu_{en}$ = electron-neutral collision frequency
$\mathbf{u}_e$ = electron drift velocity	$\tilde{\nu}_{en}$ = electron-neutral ionization collision frequency
$u_B$ = Bohm speed $(2k_B T_e / m_i)^{1/2}$	$\nu_{ew}$ = electron-wall collision frequency
$\mathbf{u}_i$ = ion drift velocity	$\nu_{i\beta}$ = coulomb collision frequency for i- $\beta$ ion pair
$\mathbf{u}_\beta$ = drift velocity of ion species $\beta$	$\Phi_s$ = electron energy loss from inelastic collisions with species "s"
$\mathbf{v}$ = particle velocity	$\phi$ = non-dimensional excitation energy loss
$Y$ = sputtering yield	$\phi$ = plasma potential
$Z$ = charge state	$\phi_T$ = thermalized plasma potential
$M_{i\beta}$ = Mach number, $v_i / (k_B T_\beta / m_\beta)^{1/2}$	$\chi$ = first conjugate harmonic function
$m_{i(e)}$ = mass of ion (electron)	$\Psi$ = Mach number function for i- $\beta$ coulomb collisions
$\dot{m}_{b(A)}$ = beam (anode) mass flow rate	$\psi$ = second conjugate harmonic function
$\dot{n}$ = electron-impact ionization rate	$\omega_{ce}$ = electron cyclotron frequency
$\hat{\mathbf{n}}$ = normal unit vector	$\Omega_e$ = electron Hall parameter
$n_{i(e)}$ = ion (electron) number density	
$n_\beta$ = number density ion species " $\beta$ "	
$r, z$ = radial, axial dimensions	

## I. Introduction

**H**all thrusters provide an attractive combination of thrust and specific impulse for a variety of near-earth missions. In many cases these systems allow for significant reductions in propellant mass and overall system cost compared to conventional chemical propulsion. The range of thrust and specific impulse attainable by these thrusters makes them applicable also to a variety of NASA science missions. Science missions however, such as those considered by NASA's Discovery Program for example, require typically wider throttling and longer thruster throughput compared to near-earth applications.<sup>1,2</sup> A critical perceived risk about the application of Hall thrusters to science missions is their throughput capability. Specifically, there are two major wear processes known to exist in Hall thrusters that can limit their applicability to NASA missions, erosion of the acceleration channel and erosion of the hollow cathode.

Multiple approaches are currently being demonstrated that address this challenge. NASA's Science Mission Directorate In-Space Propulsion Technology Program has been supporting since mid-2000 the development of a low-cost, long-life, high voltage, Hall accelerator (HiVHAc) at the NASA John Glenn Research Center (GRC). To address the risk on throughput capability, this thruster incorporates an innovative discharge channel replacement technology as a means of extending its life.<sup>3,4</sup> The first laboratory HiVHAc thruster built and tested, the NASA 77-M,<sup>5</sup> was designed and manufactured by Aerojet. In 2007, NASA GRC teamed with Aerojet to design and fabricate a flight-like HiVHAc engineering model thruster that incorporated the channel replacement life-extending innovation. In 2008 the NASA-103M.XL<sup>6</sup> had accumulated >4,700 h at 700 V in a wear test performed at NASA GRC.<sup>7</sup>

More recently, Aerojet and Lockheed Martin Space Systems (LMMS) Company successfully extended the QLT of the qualification model 4.5-kW BPT-4000 beyond 10,400 h.<sup>8</sup> The BPT-4000 has fixed insulators and a magnetic design for high efficiency and long life. Post-test assessment of the data showed no measurable erosion of the acceleration channel walls from 5,600 h to 10,400 h indicating that the thruster reached a "zero" erosion configuration. This configuration will be referred to hereinafter as the "steady-state" configuration. The QLT results have, potentially, breakthrough implications for NASA. They imply that, if properly designed, the service life of Hall thrusters can be extended to (or exceed) that of ion thrusters thereby retiring the perceived risk associated with their throughput capability.

The detailed physics that led to this significant reduction of the erosion in the BPT-4000 was not identified upon the conclusion of the QLT. As part of their development of Hall thrusters, Aerojet created a semi-empirical 2-D erosion model and the company reports excellent agreement with measured erosion profiles.<sup>8</sup> While the 2-D erosion

model does not capture the detailed physics, the QLT showed that the Aerojet design<sup>9</sup> provided the basis for efficient operation and low steady-state erosion.

The QLT has significantly exceeded the requirements for most commercial or military missions.<sup>10</sup> Because many NASA missions require long operational times, high throughput, and a wide range of operating conditions, a rigorous understanding of the erosion physics must be attained. Such understanding is important because it must be demonstrated unambiguously that ground test observations were not “anomalous” and that thruster life projections based on empirical scalings and/or semi-empirical models alone will be valid (or not) for the wide throttling requirements of NASA science missions. Also, it would reduce any risk perceived by mission teams and would allow for probabilistic life analyses.

To meet this need the Jet Propulsion Laboratory (JPL) has been supporting an advanced modeling and simulation activity for Hall thrusters. The modeling activity at JPL complements a life modeling program on ion thrusters and hollow cathodes that has been ongoing for several years now at the Laboratory. Regarding the recent erosion trends in the BPT-4000, it was recognized early at JPL that to fully understand such physics one must account, at minimum, for the two-dimensional (2-D) distribution of the electric field near the eroding surfaces, the sheath physics there, and the local topology of the magnetic field. To accomplish this, it is required usually that the solution to an extensive system of governing laws for the Hall thruster plasma in two or three dimensions is obtained. Therefore, the activity employed initially “HPHall” (Hybrid-Particle-in-Cell Hall), a 2-D plasma solver for Hall thrusters that was developed originally by Fife and Martínez-Sánchez<sup>11</sup> and later upgraded to HPHall-2 by Parra and Ahedo.<sup>12</sup> Additional algorithm advancements including a new erosion sub-model were also completed at JPL.<sup>13,14,15</sup> The HPHall-2 simulations exposed a limitation of the code that prohibited its application to explain the erosion physics in the steady-state configuration of the BPT-4000. The limitation was due to a fundamental assumption that formed the basis for its development, the so-called quasi-one-dimensional (quasi-1D) approximation for electrons,<sup>11</sup> that does not permit the numerical simulation of the thruster plasma in the specific magnetic field topology exposed by the erosion of the BPT-4000 channel. The importance of understanding the erosion physics motivated the development of a new Hall thruster plasma solver at JPL, dubbed “Hall2De,”<sup>16</sup> that is not limited by the quasi-1D approximation.

Hall2De is a 2-D computational model of the partially-ionized gas in Hall thrusters that employs the full vector form of Ohm’s law with no assumptions regarding the rate of electron transport in the parallel and perpendicular directions of the magnetic field. The model is a descendant of OrCa2D, a 2-D computational model of electric propulsion hollow cathodes that employs a mix of implicit and explicit algorithms to solve numerically the conservation laws for the partially-ionized gas in these devices.<sup>17,18</sup> Excessive numerical diffusion due to the large disparity of the transport coefficients in the two directions is evaded in Hall2De by solving the equations in a computational mesh that is aligned with the magnetic field. To the best of our knowledge, Hall2De is the first computational model of Hall thrusters to employ MFAM, and is a capability that was largely motivated by the need to assess the life capability of Hall thrusters in complicated magnetic field topologies.

Hall2De has been used to simulate the BPT-4000 with the goal to identify the physics that led to the erosion trends observed during the Aerojet/LMMS QLT and our findings are presented in this paper. The paper is organized as follows. Section II provides an overview of Hall2De and describes recent physics upgrades that have been implemented in the code. A more detailed description of the code has been provided in Ref. 16. Section III discusses comparisons between numerical simulation results and a variety of plasma and performance measurements obtained at JPL, in two different geometrical configurations of the acceleration channel. We shall be referring to these configurations hereinafter as the “1200-h” and “steady-state” channel geometries. The two geometries emulate closely the eroded channel walls after ~1200 h of operation and the “zero-erosion” configuration, respectively. We shall be referring also to the beginning-of-life (BOL) configuration, which for the purposes of this paper will represent the nominal geometrical design of this thruster at zero hours of operation. In Section IV we compare computed erosion rates between the 1200-h and steady-state geometries, explain the basic physics that produced them, and conclude with an assessment of our plasma model uncertainties on the computed erosion rates.

The Hall2De numerical simulations at JPL reveal that several changes were induced in the plasma as portions of the magnetic field, buried into the dielectric material in the BOL design of this thruster, became exposed to the plasma as the acceleration channel receded from its original geometry to its steady-state configuration. Collectively, the induced changes of the plasma properties constituted an effective shielding of the channel walls from ion bombardment. Because all such changes in the behavior of the plasma near the eroding surfaces have been found to be driven by the magnitude and topology of the magnetic field there, we call this wear-reducing mechanism “magnetic shielding.”

## II. The 2-D Axisymmetric MFAM Code “Hall2De”

### A. General description of the code and motivation behind its development

Because the fundamental principle behind the acceleration of ions in Hall thrusters is based on operating the accelerator at high electron Hall parameter ( $\Omega_e \gg 100$ ), the diffusion of mass and heat for the electron flow in the direction parallel to the magnetic field is much greater (by  $\sim \Omega_e^2$ ) than that in the perpendicular direction for most of the channel region. This leads to the “equipotentialization” and “isothermalization” of the lines of force<sup>19</sup>: streamlines of the magnetic vector field are, approximately, also lines of constant “thermalized” potential  $\phi_T = \phi - T_e \ln(n_e)$  and constant electron temperature. Numerically, this may allow for the solution of the plasma potential and electron temperature in a (quadrilateral) computational cell that is bounded by two adjacent lines of force rather than one with arbitrary dimensions. The so-called quasi-1D approximation formed the basis for the development of a number of 2-D computational models of Hall thrusters in existence today such as HPHall. HPHall uses a Particle-in-Cell (PIC) - Direct Simulation Monte Carlo method for ions in 2-D axisymmetric geometry, and was developed by Fife and Martínez-Sánchez in the late 90s.<sup>11</sup> Since then it has provided invaluable insight into Hall thruster physics at various institutions of academia, industry and government.

A desired computational capability for Hall thrusters at JPL is the assessment of erosion of the channel walls near regions of the thruster that may contain complex magnetic field topologies. For example, it is possible that excessive erosion of the acceleration channel may expose magnetic field arrangements in which a line of force begins and ends at the same surface rather than traversing the channel. In such regions the quasi-1D approximation cannot be used to simplify the numerical approach for the solution of the electron equations. A fully-2D electron solver is necessary in such cases. A main challenge however with such solvers is excessive numerical diffusion that is caused by the large disparity of the transport coefficients parallel and perpendicular to the magnetic field. This is evaded by discretizing and solving the equations on a computational mesh that is aligned with the magnetic field. MFAM is a long-standing computational approach for simulating highly anisotropic plasmas (e.g. see Refs. 20, 21, 22, 23, 24) and is the approach followed in Hall2De.

Hall2De has been under development at JPL since late 2009.<sup>16</sup> It is a physics-based computational model of the partially-ionized gas produced by Hall thrusters that employs the full vector form of Ohm’s law with no assumptions regarding the rate of electron transport in the parallel and perpendicular directions of the magnetic field. The conservation equations, numerical methodology and preliminary simulation results have been presented in detail in Ref. 16. Here we provide a brief overview of the code and describe physics and numerical upgrades that have been made to the code since our 2009 report. For convenience and clarity we shall refer to the version of Hall2De described in Ref. 16 as the “’09 version.”

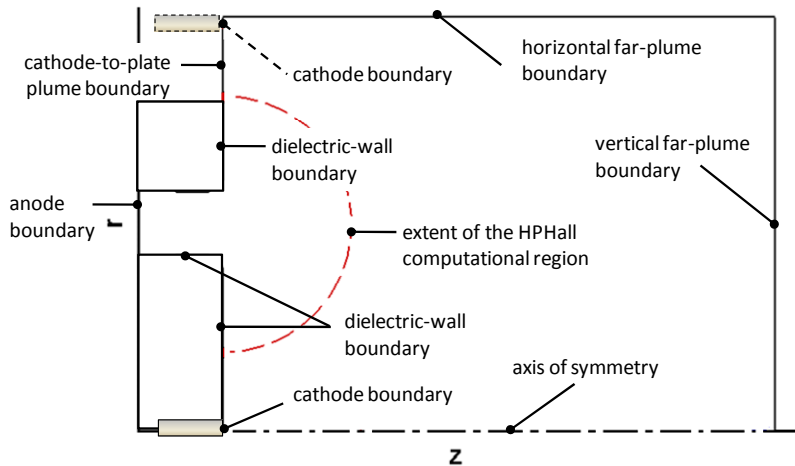


Figure 1. Schematic of the computational region and naming conventions for the boundary conditions (BC) in the MFAM code Hall2De.

Although there are many similarities with other hybrid-based codes, there are also several distinctive features of Hall2De both in the physics and the numerical approach. Such features have been incorporated in the code after many lessons learned from Hall thruster simulations over the last decade or so. Due to the wide use of HPHall both

at JPL and other institutions it may be most instructive to the community to outline the major distinctions between Hall2De and HPHall. There are four:

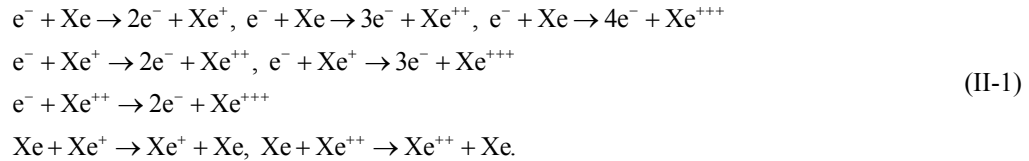
- 1) Discretization of all conservation laws on MFAM allowing for the assessment of erosion in regions with complex magnetic field topologies. The MFAM also allows for the self-consistent simulation of the plasma in the near-anode region; unlike HPHall, there is no magnetic field streamline in this region of Hall2De upstream of which the conservation laws for the plasma are not solved self-consistently.
- 2) Numerical solution of the complete vector form of Ohm's law, accounting for electron transport parallel and perpendicular to the magnetic field.
- 3) Numerical solution of the heavy-species conservation equations that are not based on discrete-particle methods (eliminating the inherent statistical fluctuations associated with such methods)
  - (a) ions are treated as an isothermal, cold (relative to the electrons) fluid accounting for the drag force and ion-pressure gradient,
  - (b) atomic species (neutrals) are treated as part of a collisionless gas and their evolution in the computational domain is computed using line-of-sight formulations that accounts for ionization.
- 4) Large computational domain that extends several times the thruster channel length in the axial direction, and encompasses the cathode boundary and the axis of symmetry.

The larger physical domain allows us to incorporate the hollow cathode boundary self-consistently. Also, although beyond the scope of this paper, the larger physical domain will allow us in the future to follow the electron flow from the cathode to the channel avoiding the modification of the transport coefficients and Hall parameter that is commonly imposed in regions of the far plume. A schematic of the Hall2De physical domain with naming conventions for the various boundaries are provided in Figure 1. The typical extent of the computational region in an HPHall simulation is also shown for comparison.

## B. Physics, numerical approach and recent augmentations in Hall2De

### 1) Ions

The evolution of ions in Hall2De is computed using a hydrodynamic approach based on the assumption that the ion gas constitutes an isothermal, cold (relative to the electrons) fluid. The justification and empirical support<sup>25</sup> for the ion-fluid approximation has been discussed in Ref. 16. The momentum and ion continuity equations for the ions account for multiple-ionization collisions, including triply-charged ions. Presently, Hall2De accounts for the following reactions:



The reaction that yields triply-charged ions from an electron collision with a singly-charged ion was recently included in the '09 version of the code, and is based on cross-sectional data provided in Ref. 26. The momentum equation (Eq. (II-2)) includes the drag force on ions, imposed on them due to their elastic and inelastic collisions with other heavy species that may be present in the simulation domain, and the ion pressure-gradient force:

$$n_i m_i \frac{D\mathbf{u}_i}{Dt} = q_i n_i \mathbf{E} - \nabla p_i + \mathbf{R}_i + \tilde{\mathbf{I}}_i \tag{II-2}$$

where  $\mathbf{R}_i$  and  $\tilde{\mathbf{I}}_i$  represent the elastic and inelastic contributions to the transport of ion momentum, respectively. For  $\mathbf{R}_i$ , the '09 version of the code accounted only for the drag due to collisions with neutrals. The code has been updated to include contributions from coulomb collisions of ions of different charge states  $Z$ :

$$\mathbf{R}_i^{\text{coulomb}} \approx -v_{i\beta} n_i m_i (\mathbf{u}_i - \mathbf{u}_\beta) \tag{II-3}$$

where,

$$v_{i\beta} = 2v_{i\beta,0} \left[ \frac{3\sqrt{\pi}}{2} \frac{\Psi(M_{i\beta}) - x\Psi'(M_{i\beta})}{2M_{i\beta}^3} \right] \quad v_{i\beta,0} = \frac{(Z_i Z_\beta)^2 e^4 n_\beta \ln \Lambda_{i\beta}}{3(2\pi)^{3/2} \epsilon_0^2 (k_B T_i)^{3/2} \sqrt{m_i}} \quad (\text{II-4})$$

$$\Psi(x) \equiv \frac{2}{\sqrt{\pi}} \int_0^x \exp(-y^2) dy.$$

The ion conservation laws are closed with conditions specified at all boundaries in Figure 1. At the anode and dielectric-wall boundaries the Bohm condition is prescribed for the speed with which the ions exit the physical domain (i.e. at entry to the sheath). At the plume boundaries the ions are allowed to flow out of the system freely (gradients of the two velocity components are set to zero). Reflection boundary conditions are set at the axis of symmetry.

Hall2De solves numerically the non-conservative form of the ion momentum equation using a first-order upwind scheme for the velocity field. The equation is marched forward in time explicitly. The velocities are defined at the vertices of each quadrilateral computational cell. Bilinear interpolation is used to define forces at vertices from their primitive values at the cell edges and to define scalar quantities at vertices from their primitive values at the cell centers.

### 1) Electrons

The electron population in Hall2De is treated as a fluid. The electron momentum equation in the absence of the viscous terms is given in vector form by

$$n_e m_e \frac{D\mathbf{u}_e}{Dt} = -en_e(\mathbf{E} + \mathbf{u}_e \times \mathbf{B}) - \nabla p_e + \mathbf{R}_e \quad (\text{II-5})$$

where the friction force  $\mathbf{R}_e/n_e$  for electrons is related to the integral of the collision term in the electron distribution function and the electron momentum. In the absence of high-frequency electron dynamics the electron inertia may be neglected. Then one obtains the vector form of Ohm's law as follows:

$$E_{\parallel} = \eta j_{e\parallel} - \frac{\nabla_{\parallel} p_e}{en_e} + \eta_{ei} j_{i\parallel} \quad E_{\perp} = \eta(1 + \Omega_e^2) j_{e\perp} - \frac{\nabla_{\perp} p_e}{en_e} + \eta_{ei} j_{i\perp}, \quad (\text{II-6})$$

expressed here in the frame of reference of the magnetic field (with “ $\parallel$ ” and “ $\perp$ ” denoting parallel and perpendicular components respectively). Equations (II-6) imply the approximation  $\mathbf{u}_e \gg \mathbf{u}_i$  (in addition to  $\mathbf{u}_e \gg \mathbf{u}_n$ ) and thus  $\mathbf{R}_e \approx -n_e m_e \nu_e \mathbf{u}_e$  with the total collision frequency “ $\nu_e$ ” including the contributions from collisions of electrons with all other species.

It has also been suggested that the diffusion of electrons in Hall thrusters is enhanced in a non-classical manner, e.g. by plasma turbulence. Many attempts to capture this enhancement in numerical simulations with HPHall and similar codes have been made through the use of an effective collision frequency, which we term here “ $\nu_\alpha$ ”. Fife and Martínez-Sánchez proposed originally<sup>11</sup> that  $\nu_\alpha$  in Hall thrusters may be based on Bohm's 1/B scaling for the cross-field mobility,<sup>27</sup> and used a coefficient  $\alpha$  to enhance the total collision frequency for the electrons while retaining the proportionality of  $\nu_\alpha$  with  $\omega_{ce}$ . In this paper we have imposed the generalized function

$$\nu_\alpha = \alpha(r, z) \omega_{ce}, \quad (\text{II-7})$$

allowing  $\alpha$  to vary spatially everywhere in the simulation region. As we shall show later in the paper numerical simulations with Hall2De that were guided largely by plasma data suggest large deviations of  $\alpha$  from a constant value and therefore little to no correlation of  $\nu_\alpha$  with  $\omega_{ce}$ . Thus, in this paper we refrain from any suggestions that “Bohm physics” persist anywhere in the channel or in the plume region of the thruster until strong evidence to the contrary emerges.

During their azimuthal drift electrons collide with walls also and this was proposed (originally by Morozov<sup>19</sup>) to be one more process that affects the transport of electrons in the acceleration channel. In numerical simulations of Hall thrusters this additional transport mechanism has been accounted for through the addition of another effective

collision frequency,  $\nu_{ew}$ . Because Ohm's law in computational models that make use of the quasi-1D assumption (like HPHall) is solved between adjacent field lines, an average value is used commonly in these models. That is, the two streamlines and the two boundaries at the inner and outer walls of the acceleration channel that bound a single computational cell for the determination of the current density across magnetic field lines, also define the volume and surface areas of that element. These are then used to determine the average wall collision frequency in the acceleration channel.<sup>11</sup> Hall2De is not limited by the quasi-1D approximation and the collision of the electrons with the walls is accounted for at the collision site, i.e. the walls. Specifically, the wall collision frequency is non-zero only at the computational cells that share at least one edge with the dielectric walls of the Hall thruster, that is:

$$\nu_{ew} = u_B \frac{S_e}{1 - S_e} \frac{\Delta A}{\Delta V}. \quad (\text{II-8})$$

In Eq. (II-8)  $\Delta A$  is the surface area of revolution associated with the boundary edge of the computational cell and  $\Delta V$  is the volume of the computational cell. The secondary electron yield is denoted by  $S_e$ . In Section III-A we provide comparisons of the collision frequencies at the channel centerline and along the wall boundaries. Accounting then for all transport mechanisms the electrical resistivity and the Hall parameter are determined as follows:

$$\eta = \frac{m_e \nu_e}{e^2 n_e} \quad \Omega_e = \frac{|B|}{en_e \eta} \quad (\text{II-9})$$

where the total electron collision frequency  $\nu_e$  is defined as

$$\nu_e \equiv \nu_{ei} + \nu_{en} + \nu_{ew} + \nu_\alpha. \quad (\text{II-10})$$

The first two terms on the right of Eq. (II-10) are the classical (total) electron-ion and electron-neutral collision frequencies.

The electron energy conservation law is solved for the electron temperature (expressed in eV) and is given by

$$\frac{3}{2} en_e \frac{\partial T_e}{\partial t} = \mathbf{E} \cdot \mathbf{j}_e + \nabla \cdot \left( \frac{5}{2} T_e \mathbf{j}_e + \kappa_e \cdot \nabla T_e \right) - \frac{3}{2} T_e \nabla \cdot \mathbf{j}_e - \sum_s \Phi_s + Q_e^T. \quad (\text{II-11})$$

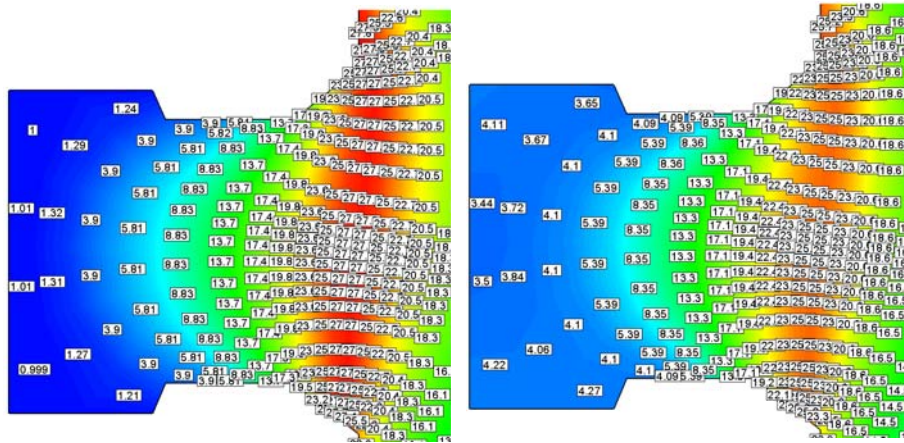


Figure 2. Hall2De has been updated with electron energy losses by excitation and with sheath BCs for the convective electron heat flux at the anode, allowing for more accurate solutions of the electron temperature in the near-anode region. Left: Only ionization losses and Dirichlet BCs for  $T_e=1$  eV as implemented in the '09 version of Hall2De . Right: With self-consistent excitation losses and sheath BCs at the anode as revised in the present version of Hall2De. The contours and boxed values depict electron temperature in eV.

The last term on the right represents the energy exchange per unit time between electrons and the heavy species<sup>28</sup> due to deviations from thermal equilibrium, and is proportional to  $n_e(m_e/m)\nu_{ei}(T_e-T_i)$  for ions and  $n_e(m_e/m)\nu_{en}(T_e-T_n)$

for neutrals. In Hall thrusters it is usually a small contribution to the total electron energy. Inelastic energy losses are accounted for by the following terms:

$$\sum_s \Phi_s = e(\varphi' - 1)(\dot{n}\zeta)_{en}^+ + e \sum_{Z=1}^3 \left[ (\dot{n}\zeta)_{en}^{Z+} + \frac{3}{2} Z T_e \right] + e \left[ (\dot{n}\zeta)_{ei}^{2+} + \frac{3}{2} T_e \right] + e \left[ (\dot{n}\zeta)_{ei}^{3+} + \frac{3}{2} T_e \right] \quad (\text{II-12})$$

where

$$\varphi' \equiv \frac{\varphi}{\zeta_{en}^+} = 1 + \frac{\tilde{a}\zeta_{en}^+}{a\zeta_{en}^+} = A_0 \exp(-A_1 \zeta_{en}^+ / T_e) + A_2 \quad \dot{n}_{es}^{Z+} = n_e (n_s a \zeta)_{es}^{Z+} \quad (\text{II-13})$$

and  $a = \langle \sigma v_e \rangle$  for the impact ionization between electrons and species “s”. Electron excitation losses are included in the first term of Eq. (II-12). Presently, these losses account only for ground-state transitions. The excitation loss rate is a term that has been added in the present version of Hall2De and is based on a fit to a solution derived by Dugan, et al.<sup>29</sup> with coefficients  $A_0=0.6$ ,  $A_1=0.304$  and  $A_2=1$  (see also Ref. 11 for the fitting function).

Another addition that has been made in the present version of the code is related to the anode BC for the convective heat flux,  $\mathbf{j}_e T_e$ . The '09 version incorporated Dirichlet BCs for the temperature at the anode boundary. The present version employs sheath BCs assuming an electron-repelling sheath at the electrode. Such BCs have been described numerous times elsewhere (e.g. see Ref. 30). The revised BCs no longer depend on a specification of the plasma temperature at the anode boundary, which in previous simulations with Hall2De practically determined the solution of  $T_e$  in this (near-anode) region. Figure 2 compares the solution before (left) and after (right) the implementation of excitation energy losses and sheath BCs in the BPT-4000 acceleration channel.

The equations for the electrons are closed with BCs at all surfaces in Figure 2. For all dielectric-wall boundaries a zero-current condition is imposed,  $\mathbf{j}_{e\perp} + \mathbf{j}_{i\perp} = 0$ . At the anode a Dirichlet condition specifies directly the voltage at its discharge value. For the simulation cases that are presented in this paper this value is 300 V. A Dirichlet condition is also imposed at the cathode with a value of 10 V. For the electron energy BCs the convective heat loss follows the formulations of Hobbs and Wesson<sup>31</sup> for the potential drop in a sheath with secondary electron emission. The secondary electron yield  $S_e$  must be provided for the specific material that is being simulated. The energy equation is solved in a semi-implicit fashion; the thermal conduction term is implicit whereas all other terms are evaluated at the previous time-step.

The numerical approach followed in Hall2De for the transport of electrons is to solve the electron equations in the frame of reference of the magnetic field, in two dimensions. Specifically, the plasma potential is solved by combining the equation for current conservation and Ohm's law into one equation and discretizing on a computational mesh that is aligned with the magnetic field lines. Numerical diffusion is reduced by assuming that cell edges are exactly either parallel or perpendicular to the magnetic field lines (Figure 3 middle). The accuracy of the solution is then dependent upon the extent of the spatial deviations of the mesh from the true lines of constant potential and stream functions  $\chi$  and  $\psi$ . Here,  $\chi$  and  $\psi$  are the commonly-used set of conjugate harmonic functions satisfying the Cauchy-Riemann conditions for the radial and axial components of the magnetic field. A set of such lines in the vicinity of the acceleration channel of a 6-kW laboratory Hall thruster are shown in Figure 3 left. The corresponding MFAM for this thruster is shown in Figure 3 right. The equation for the plasma potential equation is solved implicitly.

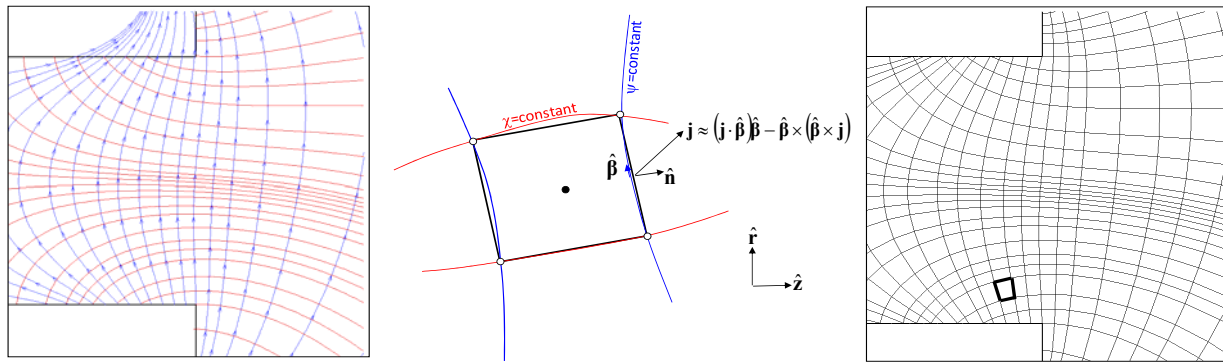


Figure 3. Left: A set of lines of constant stream function ( $\psi$ ) in blue (streamlines of the magnetic field) overlaid by lines of constant potential function ( $\chi$ ) in red, in the vicinity of the acceleration channel in a 6-kW Hall thruster. Middle: Each edge of a computational cell in Hall2De is closely aligned with either a  $\chi$ -line or a  $\psi$ -line. Right: corresponding finite-element computational mesh.

## 2) Neutrals

The neutral gas in most Hall thrusters is in the free-molecule regime. A new algorithm that is not based on discrete-particle statistics was developed for Hall2De to determine the density of neutrals.<sup>32,33</sup> The algorithm takes advantage of the fact that almost all neutral particles in this rarefied medium proceed along straight-line, constant-velocity trajectories until they are either ionized, strike a wall, or leave the physical domain. The algorithm assumes that the particle velocity distribution function for neutrals emitted from a given surface remains unchanged except for a scale factor that reflects the loss of neutrals to ionization. Then we solve for the neutral gas density by integrating forward in time the linear Boltzmann equation in the absence of any forces on the particles:

$$\frac{\partial f}{\partial t} + \mathbf{v} \cdot \nabla f = -\tilde{\nu}_{\text{en}} f. \quad (\text{II-14})$$

The sources of neutrals are gas inlets and isotropic, thermally-accommodated gas molecules emanating from chamber surfaces including recombined ions. Compared with the PIC method, commonly used in many plasma simulation codes like HPHall, this algorithm achieves “quiet” and smooth solutions as shown by the comparisons in Figure 4. The figure compares the neutral gas density in a 6-kW laboratory Hall thruster. It is noted that the HPHall solution shown in Figure 4 is averaged over thousands of cycles whereas the solution from the Hall2De algorithm is instantaneous.

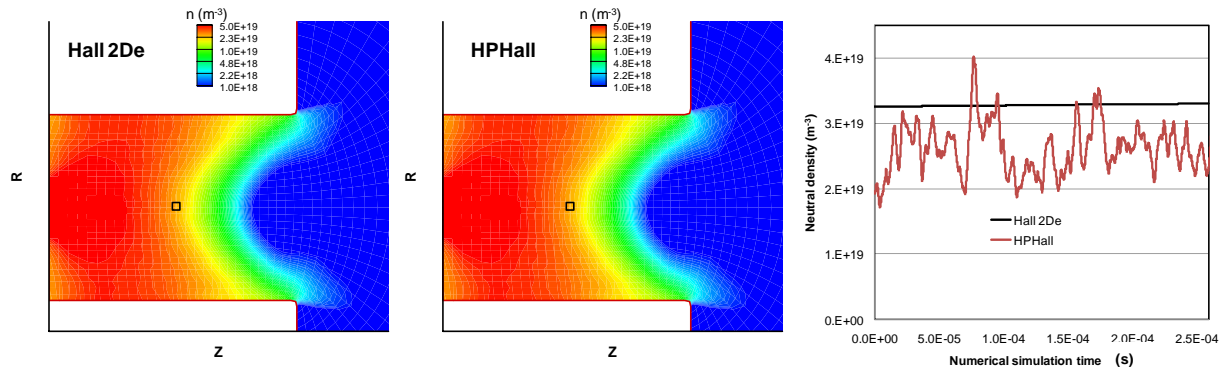


Figure 4. Left & Middle: Channel and near plume neutral gas densities calculated by the new algorithm in Hall 2De compared with time-averaged results of HPHall for a 6-kW laboratory Hall thruster. Right: Time-dependent neutral gas densities calculated by the new neutral gas algorithm in Hall2De compared with the PIC–Monte Carlo calculations from HPHall. The figure plots the solution at the computational cell outlined in the contoured plots (left & middle).

## III. Comparisons of Numerical Simulation Results and Measurements

In 2009 the BPT-4000 was operated in a large vacuum facility at JPL to evaluate the thruster’s performance at operating conditions of interest to NASA science missions and to provide in situ plasma measurements for the validation of Hall2De. In this section we present comparisons between simulation results produced by the most recent version of Hall2De and plasma measurements at various locations in the plume of the thruster. The plasma diagnostics and a more detailed description of the measurements are provided in Ref. 34. In Section III-A we describe the channel geometries simulated, and present our comparisons for the electron temperature and plasma potential along various axial and radial slices in the thruster plume. We also present comparisons with the measured performance. Section III-A concludes with a presentation of selected 2-D results and explanations of the significance of the computed trends near the walls. In Section III-B we discuss the comparisons between theory and experiment in greater detail and identify areas in our theoretical efforts that will be the focus of future investigations.

### A. Comparisons in the 1200-h and steady-state channel geometries of the BPT-4000

We have employed Hall2De to simulate the plasma and erosion in the BPT-4000 with the goal of understanding the mechanism(s) that led to the reduced wear rate during the Aerojet/LMMS QLT. Our approach has been to simulate two different channel geometries, one emulating operation early in the life of the thruster and one late in life, and then compare the erosion rates. Throughout this and subsequent sections we shall be referring to three different configurations of the BPT-4000 acceleration channel that we have constructed for our numerical simulations: (1) beginning-of-life (BOL) geometry, (2) 1200-h geometry and (3) steady-state geometry. The 1200-h

geometry resembles closely the shape of the channel walls after 1200 h of operation of the thruster in the Aerojet/LMMS QLT.<sup>8</sup> The steady-state geometry emulates closely the shape of the channel after 5,600 h; beyond this time recession of the walls by erosion had practically ceased. The three different channel geometries and reference scale lengths are shown in Figure 5.

Despite more than two decades and numerous investigations in the United States and other western countries, the true physics of the diffusion of electron heat and particle flux across magnetic field lines in conventional Hall thrusters remain elusive. Because the solution to this long-standing problem is beyond the scope of this effort our approach here has been to seek spatial variation(s) of the non-classical collision frequency  $\nu_\alpha(r,z)$  and Hall parameter  $\Omega_e(r,z)$  based on the plasma measurements. Our approach is similar to that followed by Hagelaar, *et al.*<sup>35,36</sup> This approach allows us, first, to obtain a solution for the plasma properties in the acceleration channel that we may then use to determine erosion of the acceleration channel and, second, to identify regions where the largest deviations from classical transport occur. The significance of the latter is that the results promise to guide further investigations of electron transport physics and subsequent improvements of Hall2De's physics models.

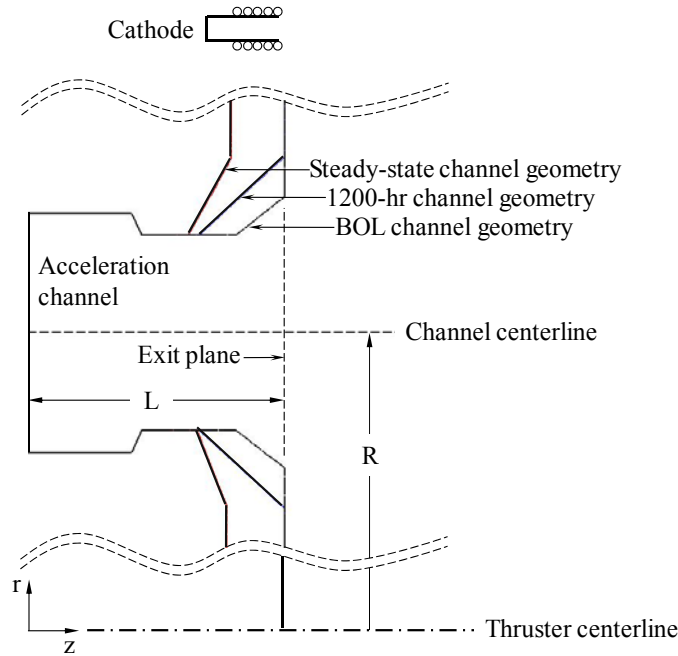


Figure 5. Schematic of the BPT-4000 acceleration channel showing the 1200-h and steady-state geometries as used in the Hall2De numerical simulations. Also shown for reference is the BOL geometry. The simulations used a mesh that was aligned with the magnetic field in BPT-4000.

We present below four simulation cases, three for the 1200-h geometry and one for the steady-state geometry. Each case is associated with different functions  $\nu_\alpha(r,z)$  and  $\Omega_e(r,z)$ . Both functions for the three cases in the 1200-h geometry are plotted in Figure 6 along the channel centerline. Also plotted in Figure 6 left and in Figure 7 are the remaining collision frequencies comprising  $\nu_e$  (see Eq. (II-10)). We note in Figure 7 that near the dielectric, electron collisions with walls can dominate the total collision frequency for a large extent of the channel. The large drop of  $\nu_{ew}$  beyond  $z/L$  for the inner channel wall compared to the outer wall seen in Figure 7 is associated with the larger values of the magnetic field near the inner surface, which in turn yield larger  $\nu_\alpha$ . These larger values are more clearly depicted in the 2-D contour plots of Figure 8 comparing  $\nu_\alpha$  (left) and  $\nu_e$  (right) for case 1.

Also, we point out that for all simulation cases with different profiles of  $\nu_\alpha$ ,  $\Omega_e(r,z)$  was determined self-consistently as the ratio  $e|B|/m_e v_e$  inside the channel but it was assigned profiles that deviated from  $e|B|/m_e v_e$  in the plume region of the thruster. With the present physics of Hall2De this assignment was found necessary to produce the best possible agreement with both the measured plasma properties and thruster performance. In the 1200-h cases,  $\Omega_e(r,z)$  was in essence relaxed to zero beyond specific magnetic field streamlines in the near-plume, analogously to the approach followed in other Hall thruster simulation codes. For example, in HPHall the Hall parameter is set equal to zero beyond the magnetic field streamline that is connected to the cathode,<sup>11</sup> which also serves as the

effective plume boundary of the code’s computational domain. The streamline beyond which this cutoff was imposed in Hall2De corresponds to  $z/L=1.31$  along the channel centerline for case 2 and  $z/L=1.69$  for cases 1 and 3.

Because the computational domain of Hall2De extends several times the channel size downstream of the thruster exit we were in a position to quantify the imposed deviation of  $\Omega_e$  from its self-consistent value. This is shown for case 1 in Figure 6 (right) by the two black lines. We find for this case that a deviation of several orders of magnitude in the far plume was required. The other two cases were found to exhibit deviations of similar order of magnitude. Therefore, the far plume remains a region of elusive physics that are currently not captured by either Hall2De or other SOA simulation codes like HPHall. In light of Hall2De’s extended plume region however, and since more than one profiles of  $v_\alpha$  and  $\Omega_e(r,z)$  have been found to produce results that are within or close to the experimental uncertainty of the plasma measurements and the observed thrust, discharge current and voltage, we sought profiles that did not relax  $\Omega_e(r,z)$  completely in the plume region. We describe one such case later in this section as it was part of the steady-state channel geometry simulations. Also, we discuss the overall implications of all the imposed profiles in greater detail in Section III-B.

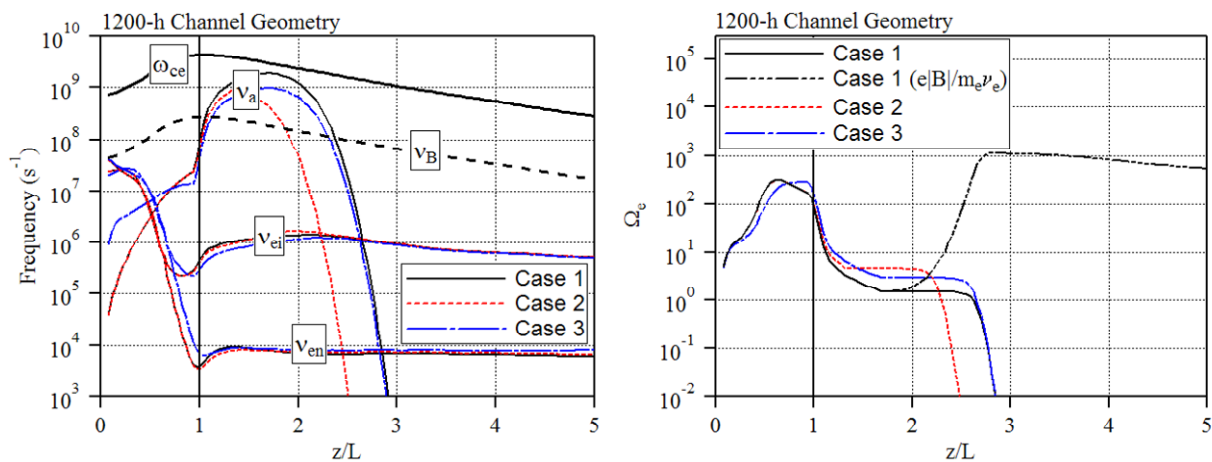


Figure 6. Numerical simulation results along the channel centerline of the 1200-h geometry (cases 1-3 of the simulations). Each case corresponds to different profiles of  $v_\alpha$  and  $\Omega_e$  as imposed in the simulations. Left: relevant frequencies. Right: Hall parameter  $\Omega_e$ . All cases in this 1200-h geometry impose a cutoff of  $\Omega_e$  in the plume region beyond a specified location downstream of the channel exit. “Case 1 ( $e|B|/m_e v_e$ )” plots  $\Omega_e$  that corresponds to the case-1 profile of  $v_\alpha$  without a cutoff, showing the location of the magnetic field streamline along the channel centerline where the cutoff is imposed.

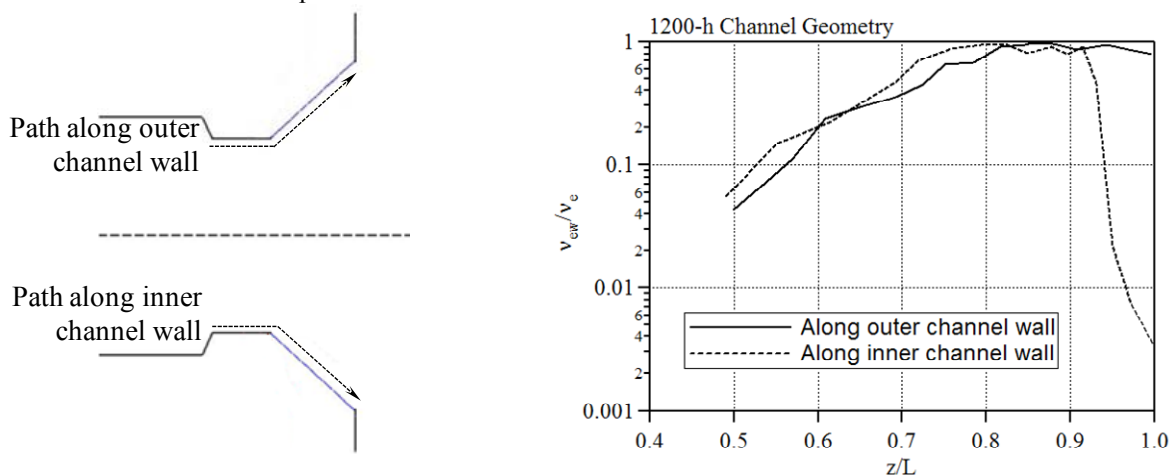


Figure 7. Contributions of electron collisions with the channel walls to the total collision frequency  $v_e$ . The collision frequency  $v_{ew}$  (see Eq. (II-8)) is implemented in Hall2De at the computational cells adjacent to the dielectric wall boundaries, as indicated in the schematic to the left. This allows us to account for the “near-wall” conductivity in this thruster. The right plot shows the ratio of  $v_{ew}$  over the total collision frequency  $v_e$  (see Eq. (II-10)), which includes  $v_\alpha$ , along the outer and inner boundaries inside the acceleration channel.

The simulation solutions of the electron temperature and plasma potential for all three cases along the channel centerline in the 1200-h geometry are compared with the plasma measurements in Figure 9. Despite the significant differences between the imposed frequency  $\nu_\alpha$ , all three cases are found to yield results that are within or close to the experimental uncertainty of the plasma measurements. Regarding thruster performance and related integrated parameters the 1200-h simulation results from all three cases are also within 3% of the measured thrust (see Table 1). The most noticeable discrepancies are associated with the thruster currents. Specifically, we find a consistent over prediction of the doubly-charged ion current fraction and an under prediction of the singly-charged fraction. These and other discrepancies between theory and experiment are discussed further in Section III-B. The beam current, mass utilization and current utilization efficiencies in Table 1 have been computed using Eqs. (III-1) as follows:

$$I_b = \sum_{Z=1}^3 I_i^{Z+} \quad \eta_m \equiv \frac{\dot{m}_b}{\dot{m}_A} = \frac{\sum_{Z=1}^3 I_i^{Z+} / Z}{e \dot{m}_A / m_i} \quad \eta_b \equiv \frac{I_b}{I_d} \quad (\text{III-1})$$

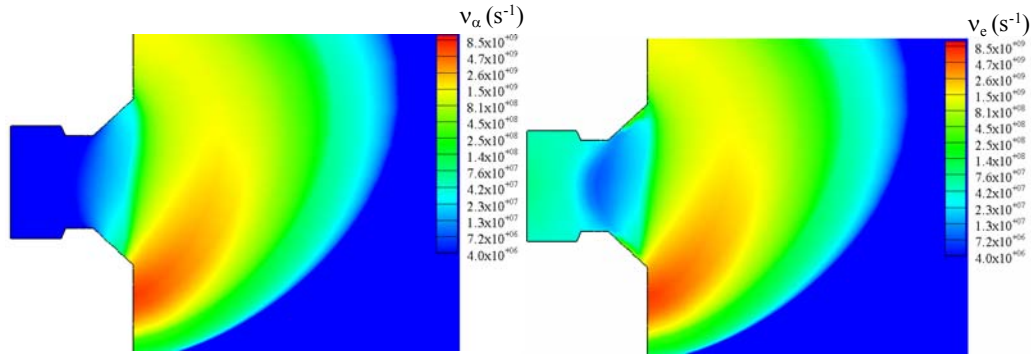


Figure 8. Contours of the non-classical collision frequency  $\nu_\alpha$  (left), implemented in the numerical simulations of the BPT-4000 for case 1, compared to the total collision frequency  $\nu_e$  (right).  $\nu_e$  accounts for classical coulomb collisions between electrons and ions, electron-neutral collisions and near-wall collisions.

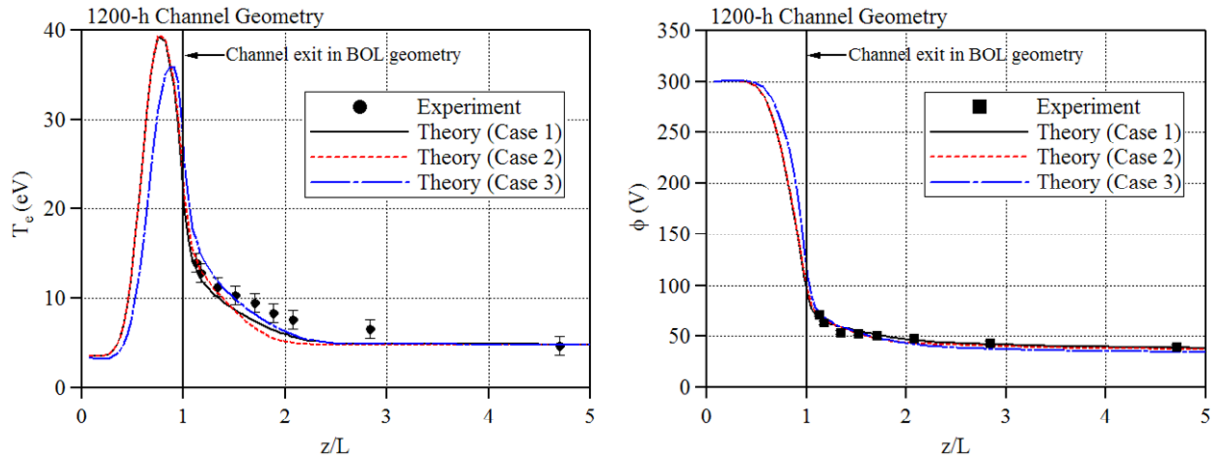


Figure 9. Comparisons between numerical simulation results and axial plasma measurements obtained along the channel centerline ( $r/R=1$ ) in the 1200-h geometry of the BPT-4000. Left: electron temperature. Right: plasma potential.

Radial comparisons between the computed results and plasma measurements have also been performed. They are shown in Figure 10 for three axial locations in the 1200-h geometry. The top-left figure shows contour plots of the plasma potential for case 1; the three radial slices along which the comparisons are made are also plotted as dashed lines. The top-right figure is the comparison closest to the acceleration channel,  $z/L=1.113$ , followed by  $z/L=2.088$  (bottom-left) and  $z/L=4.715$  (bottom-right). The simulation predicts well the plasma potential within approximately a channel height in front of the acceleration channel but the agreement is found to diminish at greater angles relative to the thrust vector. This discrepancy is discussed further in Section III-B.

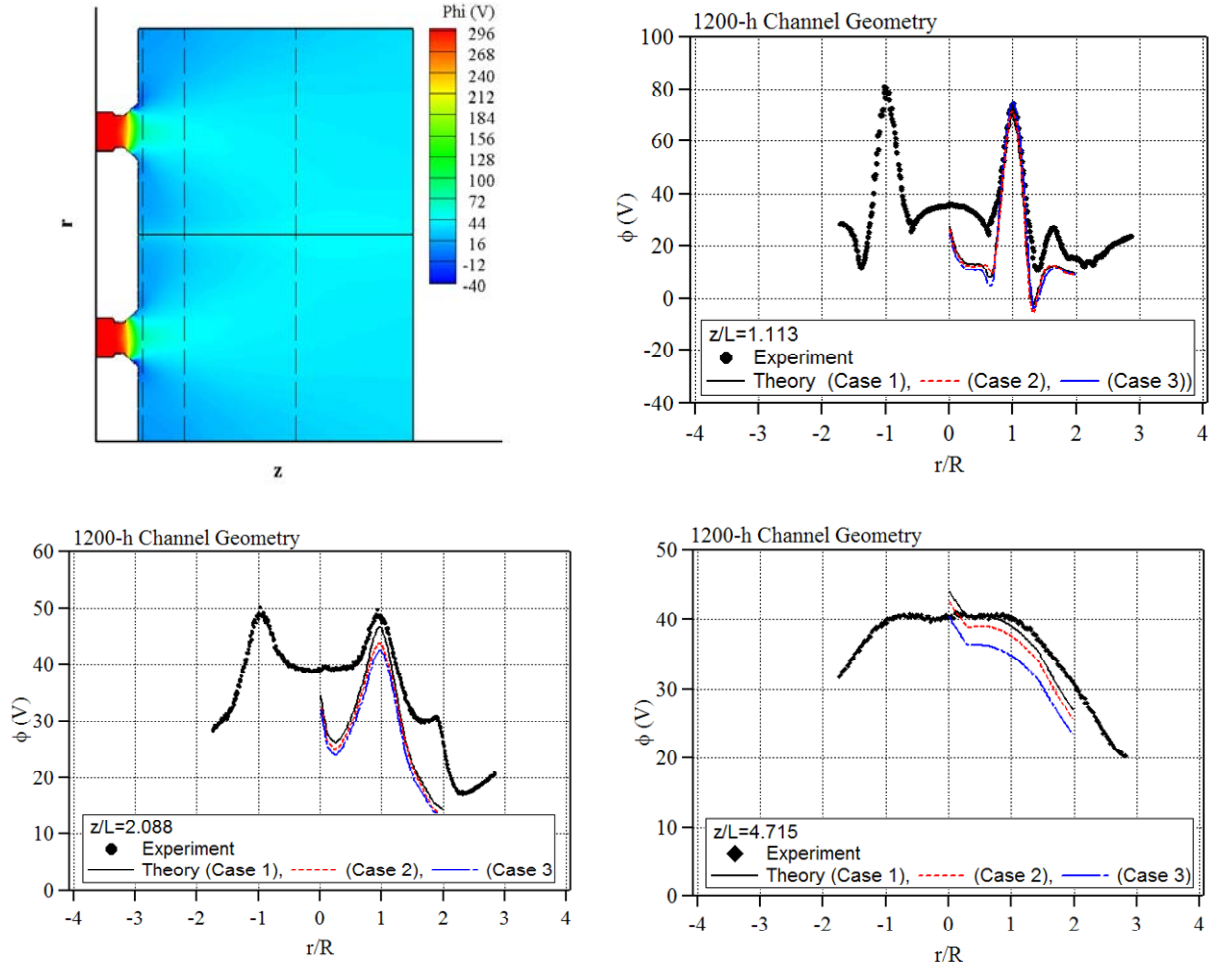


Figure 10. Comparisons between numerical simulation results and radial measurements of the plasma potential. The comparisons are made at different locations downstream of the channel exit in the near-plume of the BPT-4000 operating with the 1200-h channel geometry. Top-left: computed contours of the plasma potential for case 1 showing radial slices along which the comparisons between theory and experiment have been performed. Top-right, bottom-left and bottom-right: comparisons at  $z/L=1.113$ ,  $2.088$  and  $4.715$ , respectively.

Table 1. Performance comparisons between numerical simulation results and measurements performed at JPL<sup>34</sup> in the 1200-h and steady-state channel geometries of the BPT-4000.

Channel geometry	1200-h				Steady-state	
	Experiment	Theory (Case 1)	Theory (Case 2)	Theory (Case 3)	Experiment	Theory (Case 4)
Experiment vs. Theory						
Anode (mass) flow rate (mg/s)	14.4	14.4	14.4	14.4	14.5	14.4
Discharge voltage (V)	300	300	300	300	300	300
Discharge current (A)	15	15	15	15	15	15
Thrust (mN)	278.6	274.7	275.0	272.1	280.4	270.9
Beam current, $I_b$ (A)	12.1	12.86	12.87	12.60	12.2-12.3	13.0
Xe <sup>+</sup> current fraction, $I_i^+/I_b$	0.691	0.644	0.643	0.663	0.696	0.622
Xe <sup>2+</sup> current fraction, $I_i^{2+}/I_b$	0.241	0.315	0.316	0.302	0.204	0.332
Xe <sup>3+</sup> current fraction, $I_i^{3+}/I_b$	0.054	0.041	0.041	0.034	0.080	0.046
Xe <sup>4+</sup> current fraction, $I_i^{4+}/I_b$	0.015	NA	NA	NA	0.021	NA
Mass utilization, $\eta_m$	0.952	0.998	0.998	0.990	0.95-0.958	0.987
Current utilization, $\eta_b$	0.807	0.857	0.858	0.840	0.813-0.82	0.867

NA=not accounted for in the simulation.

Similar comparisons between theory and experiment are presented below for the steady-state channel geometry. Figure 11 left plots the relevant collision frequencies along the channel centerline including the imposed profile for  $\nu_\alpha$ ; we shall refer to this simulation as “case 4.” By utilizing the extended computational region of Hall2De we attempted in this simulation geometry to find profiles of the collision frequency  $\nu_\alpha$  and  $\Omega_e$  that produced closely the plasma and performance measurements while relaxing the stringent cutoff of  $\Omega_e$  imposed beyond a given magnetic field streamline in the 1200-h cases. The imposed profile for  $\Omega_e$  that best reproduces the experimental observations is plotted in Figure 11 right as the solid line, and is compared on the same plot with the self-consistent profile (dash-dotted line). We find that this double-humped distribution resembles qualitatively the self-consistent value of  $\Omega_e$  while reducing significantly the discrepancy between them in the plume region compared to the 1200-h cases. The axial comparisons between theory and experiment that result from these imposed profiles are depicted in Figure 12.

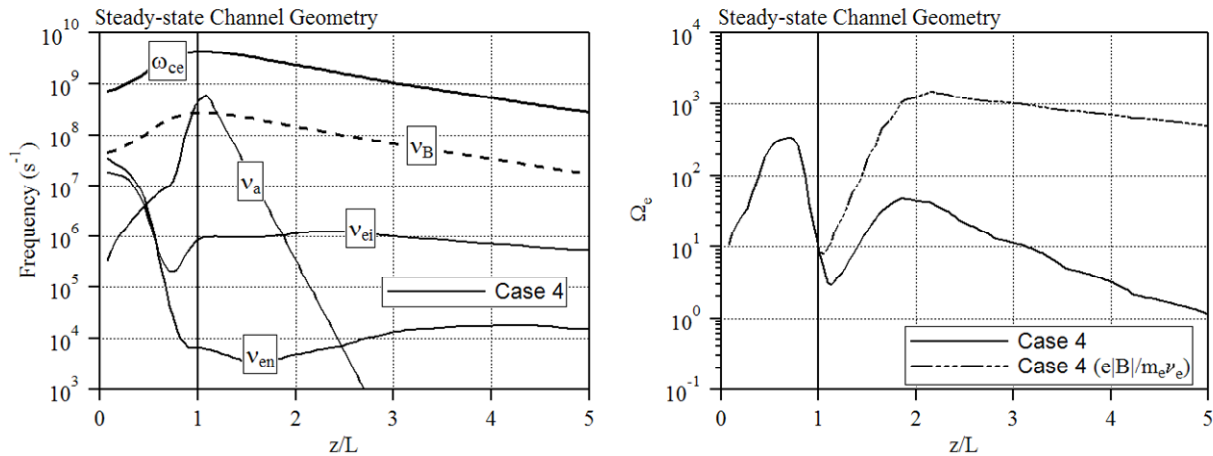


Figure 11. Numerical simulation results along the channel centerline in the steady-state geometry (case 4 of the simulations). Left: relevant frequencies. Right: Hall parameter (solid line). The dash-dotted line corresponds to the Hall parameter as computed directly from the total collision frequency  $\nu_e$ . A comparison of the two profiles quantifies the magnitude of the modification needed in the plume region to achieve correlation with the plasma measurements.

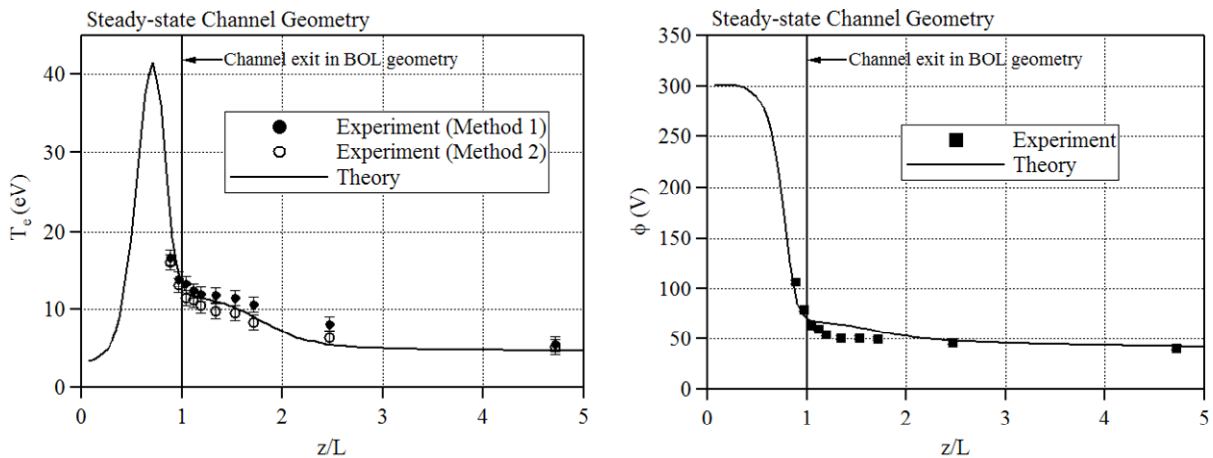


Figure 12. Comparisons between numerical simulation results and axial plasma measurements obtained along the channel centerline ( $r/R=1$ ) in the steady-state geometry of the BPT-4000. Left: electron temperature. Right: plasma potential. Method 1: directly from Langmuir probe traces. Method 2: derived from emissive probe measurements.

The radial comparisons at two different axial locations downstream of the channel exit,  $z/L=1.188$  and  $1.525$ , are plotted in Figure 13. The comparison in Figure 13 left is of particular interest since both theory and experiment display a non-monotonic profile of the electron temperature with radius. The significance of this trend is that such non-monotonicity is expected at this proximity to the channel exit due to the magnetic field topology in the region and the isothermalization of the field lines. It is also observed that the numerical simulation predicts a profile that is very similar, both qualitatively and quantitatively, to the measurement but at a different location relative to the channel. The spatial discrepancy is of the order of a few millimeters and may be caused by differences between the magnetic field model used in the simulations and the real field applied in the thruster. Also, cumulatively, probe-thruster misalignments are estimated to be of the order of 1-2 mm.

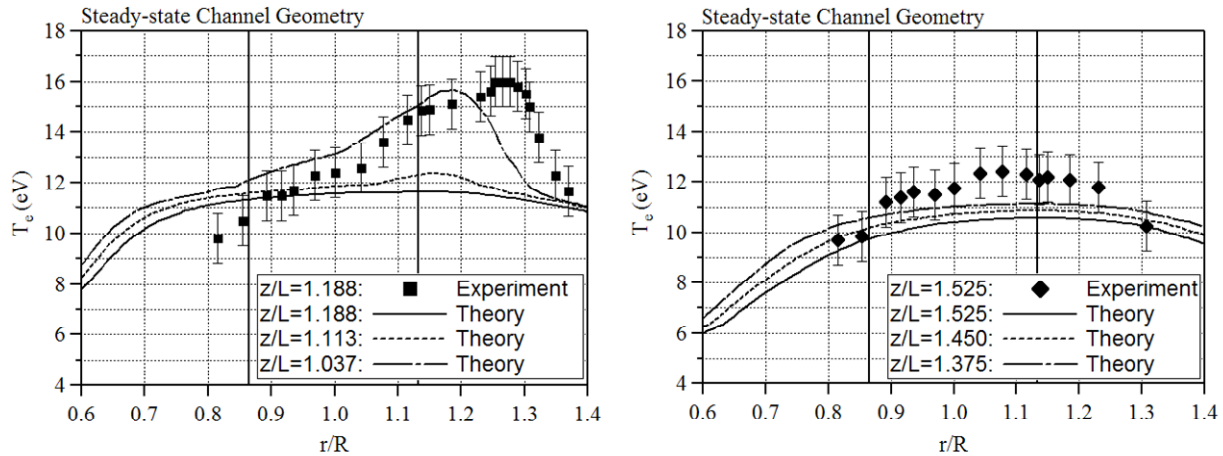


Figure 13. Comparisons between numerical simulation results and radial measurements of the electron temperature obtained at two different locations,  $z/L=1.188$  (left) and  $z/L=1.525$  (right), downstream of the acceleration channel in the steady-state geometry of the BPT-4000. The left and right vertical lines on each plot indicate the radial locations of the inner and outer walls of the channel's cylindrical section, respectively.

Contour plots in the two geometries are shown in Figure 14. The effect of the equipotentialization of the lines of force<sup>19</sup> is shown clearly in Figure 14 top. The plot compares computed plasma potential contours in the 1200-h and steady-state geometries. For example, we find only a 30-V reduction (275 to 245 V) along the outer diverging wall of the steady-state configuration compared to significant drop of 286 V in the 1200-h geometry. Thus, acceleration of ions along the diverging wall in the 1200-h is considerably higher compared to the steady-state geometry. This higher acceleration, in turn, increases the ion kinetic energy into the sheath.

The same principle that leads to the equipotentialization of the lines of force is responsible also for their "isothermalization." Then, since lines of force are nearly isothermal in the acceleration channel, the line that grazes the diverging wall and proceeds almost parallel to it is associated also with a low value of the electron temperature since such line extends deep into the acceleration channel where the electrons are considerably cooler (see also left of Figure 9 and Figure 12). For the BPT-4000 channel this is shown in Figure 14 middle comparing contours of the electron temperature in the 1200-h and steady-state geometries. The comparison shows a reduction in the maximum temperature, as much as seven times along the diverging walls. Because the electron temperature was reduced significantly along the diverging walls in the steady-state geometry we also obtained a reduction in the sheath drop across these surfaces.

A third effect seen in the steady-state geometry is largely linked to the plasma potential profile. Specifically, because the component of the electric field parallel to the diverging section of the dielectric is marginalized in the steady-state geometry, the acceleration of ions is largely axial and away from the diverging wall. This is shown by the representative velocity streamlines of singly-charged ions overlaid on the electron number density contours in Figure 14 bottom. Thus, the radial expansion of the plasma beyond the cylindrical section of the accelerator is reduced compared to that in the 1200-h geometry, and the region near the diverging wall of the steady-state geometry is populated by a much lower number of charged particles. The electron number density in the two geometries in Figure 14 bottom shows more than one order of magnitude less density in the steady-state geometry. The significance of this reduction on erosion is that the total flux to the wall is also reduced.

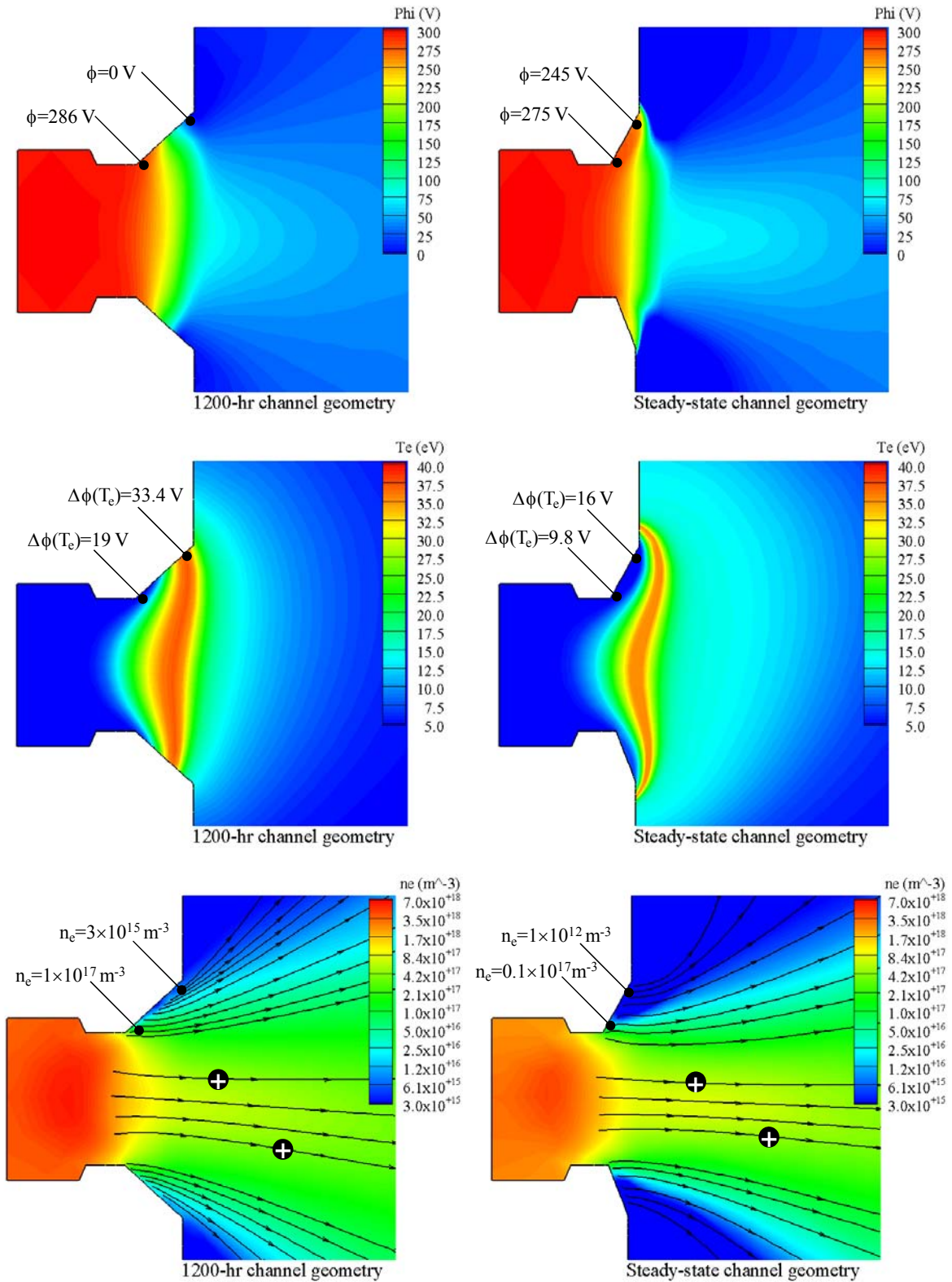


Figure 14. Comparison of the numerical simulation results in the 1200-h (left) and steady-state (right) channel geometries. Top: Plasma potential. Middle: Electron temperature. Bottom: Electron number density overlaid by representative trajectories of singly-charged ions.

## B. Discussion on the comparisons between theory and experiment

The wide range of comparisons between thruster measurements and numerical simulations that have been performed here establish the state of the validation of Hall2De and identify clearly areas in Hall2De’s physics models that require further improvement. The most evident need for better understanding is associated with the fact that a different profile of the collision frequency  $\nu_\alpha$  must be prescribed in different channel geometries and/or operating conditions, which implies that Hall2De is not yet a fully-predictive code for Hall thrusters. This has been a long-standing challenge in the numerical simulation of Hall thrusters that is more than two decades old. However, Hall2De is now at a state of development that allows us to address this challenge directly. The extended computational region and the MFAM are capabilities that were specifically developed to allow us, in part, to interrogate mechanisms pertinent to electrons transport (such as large-scale electron current paths to the acceleration channel) that cannot be captured by other SOA simulation codes.

As a precursor to a more detailed interrogation on this subject we performed a series of sensitivity simulations with different profiles of the collision frequency  $\nu_\alpha$  to identify region(s) that deviate most significantly from classical transport. The intent was to seek functional dependencies of this “non-classical” frequency here, as guided by the measurements, which could lead us to first-principles formulations of the true transport physics. Our sensitivity simulations with different profiles in the 1200-h geometry show that different functional forms of  $\nu_\alpha$  can produce similar solutions for the plasma and thruster performance. This presents a challenge in our quest of the true electron transport physics because different spatial variations of  $\nu_\alpha$ , all yielding results that are either within or close to the experimental uncertainty with the plume plasma measurements, thrust and discharge characteristics of the thruster, make correlations with true frequencies ambiguous. For example, by comparison to the electron cyclotron frequency or the Bohm ( $\nu_B = \omega_{ce}/16$ ) collision frequency (also plotted in Figure 6 and Figure 11), we find no functional similarities with the imposed  $\nu_\alpha$  that span both the acceleration channel and the near plume. Noted is the comparison of the frequencies inside the channel: although  $\nu_\alpha$  for case 3 is directly proportional to  $\omega_{ce}$  ( $\propto B$ ), cases 1 and 2 fall faster with decreasing magnetic field inside the channel. Outside the channel we find  $\nu_\alpha$  to differ significantly from  $\nu_B$  in peak magnitude *and* spatial variation, in both the 1200-h and steady-state channel geometries. Thus, although electron collisions other than those associated with classical particle interactions – such as collisions with the thruster walls – may indeed lead to distinctive transport trends inside and outside the acceleration channel, we find no correlations between  $\nu_\alpha$  and  $\nu_B$ , and are unable to identify distinct regions of this problem that can be linked unambiguously with different fractions of  $\nu_B$ . Therefore, we refrain from making any suggestions of the existence of Bohm physics as this would imply specific dependencies of transport physics on the magnetic field.

The results from our sensitivity simulations on the modification of the Hall parameter (see left of Figure 6 and Figure 11) in the plume regions suggest that processes here cannot be uncoupled from the numerical simulations of the acceleration channel; but such processes remain not well understood. The coupling of the physics in the acceleration channel and plume regions was a conclusion of our previous work (see Ref. 16) and remains unchanged based on the results of this effort. The radial comparisons between theory and experiment in the 1200-h geometry (see Figure 10) identify clearly regions where the behavior of the plasma remains elusive. Specifically, referring to Figure 15, we find that although the imposed profiles of  $\nu_\alpha$  and  $\Omega_e$  lead to good agreement with the plasma potential measurement near the channel centerline, the agreement begins to diminish away from it in the radial direction. In these high-angle regions of the thruster plume the simulation results simply reflect the expected variation of the plasma potential there as the low-density ion beam converges onto the thruster centerline. The radial gradient of the plasma potential computed by Hall2De and depicted in Figure 10 is, therefore, not surprising. However, the measurement (also shown in Figure 10) suggests a different trend with radius. This trend is most evident in the  $z/L=1.113$  and  $2.088$  locations and  $0 < r/R < 0.75$ , i.e. in the inner regions of the plume closest to the thruster walls. Of particular interest is the negligible radial electric field measured at the thruster centerline, which implies the presence of low-energy plasma. This plasma is not captured by the simulation. Using the measured values of the plasma potential and electron temperature<sup>34</sup> for  $z/L=1.113$ , and the computed

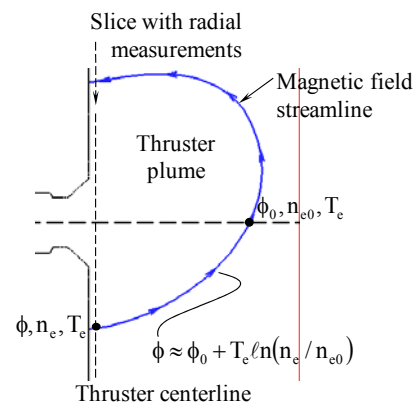


Figure 15. Schematic for the estimation of the plasma density near the thruster centerline based on measurements of the plasma potential and simulation results at the channel centerline.

values of the plasma density in the thruster beam we may estimate the density one would expect to have in these regions of discrepancy between theory and experiment. As a representative location we choose  $(r/R, z/L)=(0.4, 1.113)$  where the computed and measured values differ by approximately 20 V. Referring to Figure 15, since the plasma potential along field lines is approximately  $\phi \approx \phi_0 + T_e \ln(n_e/n_{e0})$ , we can identify a magnetic field streamline that contains this point and also crosses the channel centerline. At the channel-centerline point we use the computed values for the plasma potential, electron number density and temperature,  $\phi_0$ ,  $n_{e0}$  and  $T_e$  respectively, to estimate  $n_e$  as follows:

$$n_e = n_{e0} \exp\left(\frac{\phi - \phi_0}{T_e}\right) \approx 3.5 \times 10^{16} \text{ m}^{-3}. \quad (\text{III-2})$$

This value is approximately two orders of magnitude higher than  $\sim 5.2 \times 10^{14} \text{ m}^{-3}$  as computed by Hall2De at this location. Low-energy charge-exchange ions are a possible source for this discrepancy. Presently, such ions are not treated as a distinct species in Hall2De and as a result their concentration may be underestimated significantly in these regions of the thruster. Emission from the walls that are not presently captured by the classical wall models in Hall2De, and/or enhanced ionization not accounted for by the inelastic models in Hall2De are other candidates that may be responsible for the discrepancy. The nature of the emission characteristics and related sheath physics has been a subject of investigation for several years [e.g. see Refs. 37, 38, 39, 40 and 41] and is an area we plan to revisit in the near future since such physics may affect our simulation results in the plume regions of the thrusters but also the transport of electrons inside the acceleration channel. For example, enhanced emission of low-energy electrons from walls may alter significantly the sheath and, in turn, the electron energy balance inside the channel. With the present physics models in Hall2De the code appears to yield higher electron temperature inside the BPT-4000 channel than the values expected based, for example, on the ion current fractions (see Table 1). The current fractions are currently over predicted by Hall2De for doubly-charged ions and under predicted for singly-charged ions.

The one-on-one comparisons with the BPT-4000 measurements at JPL have identified areas of improvement in the Hall2De physics simulation capabilities but have also allowed us to obtain plasma solutions for the two channel geometries that now permit detailed assessments of the erosion rates in this thruster. For example, in the channel and near field plume, we have found values of an effective collision frequency such that, using the self-consistent value of the Hall parameter, Hall2De model results are comparable to the measurements. However, for all cases (Figures 7 and 11) it was necessary to reduce significantly or eliminate entirely the Hall parameter in the far plume in order to keep calculated potentials and electron temperatures as low in the far plume ( $z/L > 3$ ) as the measurements. In the far plume, the electron flow neutralizes the ion beam current. As discussed in Katz, *et al.*,<sup>42</sup> most of the electrons that leave the hollow cathode proceed to neutralize the ion beam current and only a small fraction of them enter the channel. Presently, the Hall2De far plume BCs impose current neutrality. This local BC requires electrons leave the computational region at the same location as the ions. Since the ions are not magnetized many electrons are forced across field lines to neutralize the beam. This current generates a substantial electric field because it is multiplied by the Hall parameter squared. One possibility is that the path for these electrons extends far outside the Hall2De computational grid and beam current neutralization occurs meters downstream of the thruster exit plane. If so, regions in the Hall2De plume that predict presently finite electron current density could sustain negligible flow of electrons, which would marginalize the contributions of the resistive electric field in these regions. Current neutralization far down stream of the channel exit is consistent with published data showing that hollow cathode coupling improved when the cathode was far from the thruster.<sup>43</sup> We plan to investigate this in the future by using a much larger computational region and a self-consistent Hall parameter.

## IV. Erosion Calculations and the Basic Physics of the Plasma at the Channel Walls

### A. Background and coefficients for the erosion rates

The sputtering erosion rate due to ion bombardment is given by,

$$\varepsilon = j_{\perp} Y \quad (\text{IV-1})$$

where the incident ion current density perpendicular to the channel wall  $j_{\perp}$  is dependent on the ion number density and the ion velocity at the wall. The sputtering yield of the channel material  $Y$  is a function of the ion impact energy

and incidence angle. Because ions must traverse a sheath at the wall before striking it, the total impact energy is the sum of the kinetic energy  $K_i = \frac{1}{2}m_i u_i^2$  the ions have acquired in the plasma upon entrance to the sheath and the sheath potential energy  $\Delta\phi$ . These dependencies may be expressed as

$$j_{i\perp} = j_{i\perp}(q_i, n_i, u_{i\perp}) \quad Y = Y(K_i + \Delta\phi, \theta). \quad (IV-2)$$

The potential energy  $\Delta\phi$ , transformed to ion kinetic energy as the plasma ions are accelerated inside the sheath towards the solid material, is computed based on the solution to the one-dimensional sheath equations in the presence of secondary electron emission. Hobbs and Wesson<sup>31</sup> showed that the sheath equations for this problem consist of a system of three non-linear equations for the electric field, sheath potential and ion Mach number. For ease of computation in the numerical simulations we employ a fit<sup>44</sup> to the Hobbs and Wesson solution as follows:

$$\frac{\Delta\phi}{T_e} = \begin{cases} \ln[C_0(1-S_e)] - C_1(1-S_e)^{-2} - C_2(1-S_e)^{-3} - C_3(1-S_e)^{-4}, & S_e < 1 - 8.3\sqrt{m_e/m_i} \\ 1.018, & S_e \geq 1 - 8.3\sqrt{m_e/m_i} \end{cases} \quad (IV-3)$$

The coefficients in Eq. (IV-3) are given by  $C_0=195.744$ ,  $C_1=1.28971 \times 10^{-4}$ ,  $C_2=-3.45464 \times 10^{-6}$  and  $C_3=3.6807 \times 10^{-8}$ . The secondary electron yield for the BPT-4000 channel material is approximated by,

$$S_e = S_{e0} + (1 - S_{e0}) \frac{T_e}{K_{e0}/2} \quad (IV-4)$$

where  $S_{e0}=0.54$  and the Maxwellian cross-over is  $K_{e0}/2=20$  V. In the simulation we use the vertex-centered ion velocities and the cell-centered ion density at each computational cell adjacent to the wall boundary to determine the total impact energy  $K=K_i+\Delta\phi$  and incidence angle  $\theta$ . Then the sputtering yield is determined using the fitting functions  $f_K(K_i+\Delta\phi)$ <sup>45</sup> for the energy dependence at zero angle of incidence and  $f_\theta(\theta)$ <sup>46</sup> for the angle dependence, as follows:

$$Y = f_\theta(\theta) f_K(K). \quad (IV-5)$$

The fitting functions  $f_K$  and  $f_\theta$  are plotted in Figure 16.

The erosion rates have been computed at three different locations along the diverging section of the BPT-4000 channel in the 1200-h and steady-state geometries. The relevant schematic is shown in Figure 17. The three locations are denoted ‘‘U’’, ‘‘M’’ and ‘‘D’’ for upstream, middle and downstream points, respectively. The rates and all relevant parameters that led to their determination are tabulated in Tables 2 and 3.

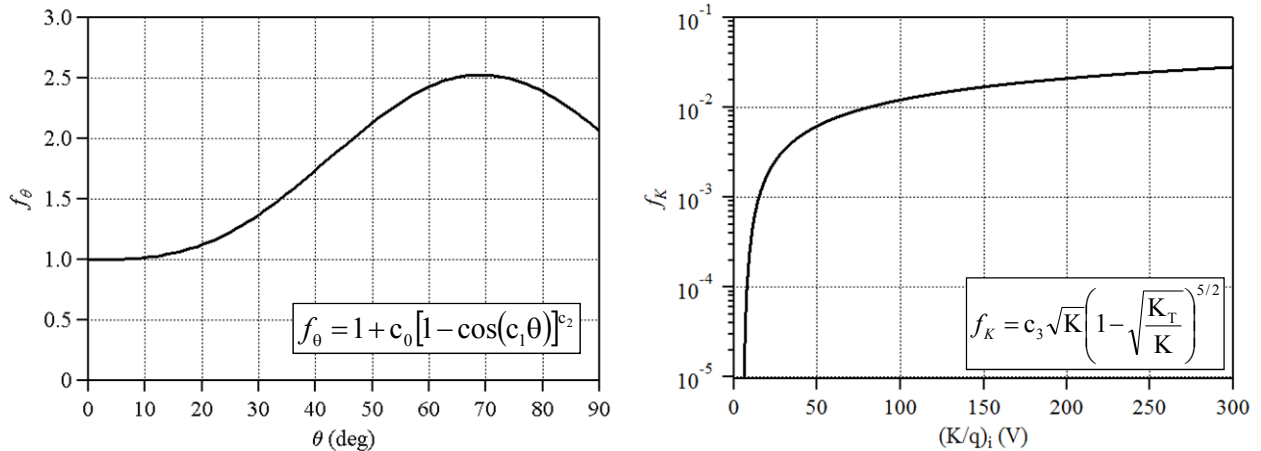


Figure 16. Fitting functions for the sputtering yield in Eq. (IV-5). The coefficients are  $c_0=0.52663$ ,  $c_1=2.60506$ ,  $c_2=1.53462$ ,  $c_3=0.0023$  and  $K_T=5.1$ .

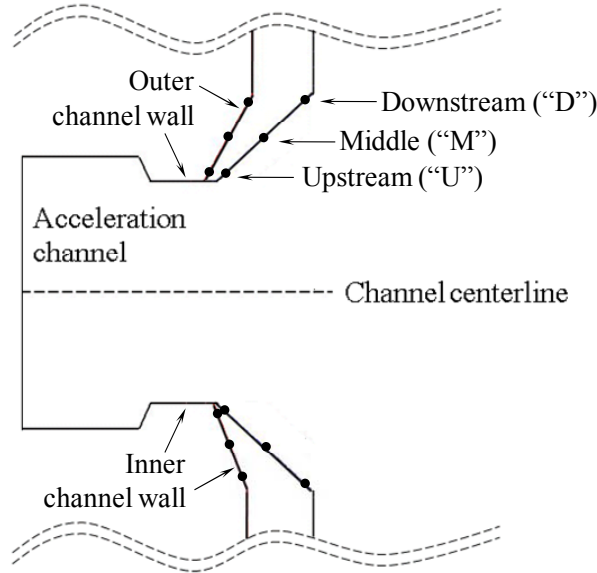


Figure 17. Locations along the diverging dielectric walls of the BPT-4000 where erosion rates have been assessed and tabulated by the numerical simulations (see Tables 2 and 3).

Table 2. Erosion rates and relevant parameters at the outer wall in the 1200-h and steady-state (SS) channel geometries of the BPT-4000.

Location along wall Channel geometry	Upstream (U)		Middle (M)		Downstream (D)	
	1200-h (Case 3)	SS (Case 4)	1200-h (Case 3)	SS (Case 4)	1200-h (Case 3)	SS (Case 4)
$T_e$ (eV)	4.5	2.2	18.7	2.2	32.8	3.7
$n_i^+$ ( $m^{-3}$ )	$1.3 \times 10^{17}$	$1.1 \times 10^{16}$	$2.3 \times 10^{15}$	$6 \times 10^{14}$	$3.4 \times 10^{15}$	$2.1 \times 10^8$
$n_i^{2+}$ ( $m^{-3}$ )	$1.9 \times 10^{15}$	$7 \times 10^{13}$	$3 \times 10^{14}$	$4.7 \times 10^{12}$	$1.4 \times 10^{15}$	$1.6 \times 10^6$
$n_i^{3+}$ ( $m^{-3}$ )	$1.5 \times 10^{12}$	$3.3 \times 10^{11}$	$1.4 \times 10^{13}$	$2.9 \times 10^{10}$	$2 \times 10^{14}$	$8.2 \times 10^{-6}$
$\phi$ (V)	285.7	275.1	165.9	269.1	$7.0 \times 10^{-2}$	245
$j_{iL}^+$ ( $A/m^2$ )	12.5	1.7	0.9	$8.4 \times 10^{-2}$	2.4	$3.8 \times 10^{-8}$
$j_{iL}^{2+}$ ( $A/m^2$ )	0.5	$3 \times 10^{-2}$	0.3	$2 \times 10^{-3}$	2.8	$7.5 \times 10^{-10}$
$j_{iL}^{3+}$ ( $A/m^2$ )	$6 \times 10^{-4}$	$2.5 \times 10^{-4}$	$2.6 \times 10^{-2}$	$2.2 \times 10^{-5}$	0.8	$6.7 \times 10^{-21}$
$(K/q)_i^+$ (V)	7.2	4.2	78.6	10.8	83.4	34.8
$(K/q)_i^{2+}$ (V)	7.6	6	63.4	13.7	69.7	43.8
$(K/q)_i^{3+}$ (V)	15.1	9.2	52.2	14.8	61.3	51.8
$\Delta\phi$ (V)	19	9.8	31.8	9.8	33.4	16
$\theta^+$ (deg)	31	29.9	55.4	44.6	51.1	54.8
$\theta^{2+}$ (deg)	31.6	35.7	52.3	48.3	48.4	58
$\theta^{3+}$ (deg)	41.5	42.4	49.4	49.4	46.3	60.3
$Y^+$ ( $\times 10^{-2} mm^3/C$ )	0.4	0.1	3.0	0.4	3.0	1.5
$Y^{2+}$ ( $\times 10^{-2} mm^3/C$ )	0.4	0.2	2.6	0.5	2.6	1.8
$Y^{3+}$ ( $\times 10^{-2} mm^3/C$ )	0.7	0.3	2.2	0.5	2.3	2.1
$\epsilon^+$ (mm/h)	$1.7 \times 10^{-4}$	$7 \times 10^{-6}$	$9.5 \times 10^{-5}$	$1 \times 10^{-6}$	$2.6 \times 10^{-4}$	$2 \times 10^{-12}$
$\epsilon^{2+}$ (mm/h)	$8 \times 10^{-6}$	$1.9 \times 10^{-7}$	$2.6 \times 10^{-5}$	$3.4 \times 10^{-8}$	$2.6 \times 10^{-4}$	$4.8 \times 10^{-14}$
$\epsilon^{3+}$ (mm/h)	$1.5 \times 10^{-8}$	$2.7 \times 10^{-9}$	$2 \times 10^{-6}$	$4.2 \times 10^{-10}$	$7.0 \times 10^{-5}$	$5 \times 10^{-25}$
<b>Total <math>\epsilon</math> (mm/h)</b>	<b><math>1.8 \times 10^{-4}</math></b>	<b><math>7 \times 10^{-6*}</math></b>	<b><math>1.2 \times 10^{-4}</math></b>	<b><math>1 \times 10^{-6}</math></b>	<b><math>5.8 \times 10^{-4}</math></b>	<b><math>2 \times 10^{-12}</math></b>

\*This erosion rate is an overestimate of the real value in the BPT-4000 QLT because the numerical simulation geometry employs a sharp corner at this location whereas in the real geometry this corner was smoothed out by the erosion. The significance of this difference is that in the simulation the corner "interrupts" magnetic field streamlines leading to potential differences around the corner that allow ions to acquire kinetic energy. By contrast, the curvature of the eroded corner in the test follows closely the curvature of the streamline around that corner; the equipotentialization of the streamline reduces the acceleration of the ions around the corner and, in turn, the kinetic energy with which they impact the surface of the thruster.

Table 3. Erosion rates and relevant parameters at the inner wall in the 1200-h and steady-state (SS) channel geometries of the BPT-4000.

Location along wall Channel geometry	Upstream (U)		Middle (M)		Downstream (D)	
	1200-h (Case 3)	SS (Case 4)	1200-h (Case 3)	SS (Case 4)	1200-h (Case 3)	SS (Case 4)
$T_e$ (eV)	6.5	12.1	34.3	9.8	14.6	12.8
$n_i^+$ ( $m^{-3}$ )	$1.2 \times 10^{17}$	$4.5 \times 10^{16}$	$1.6 \times 10^{16}$	$2 \times 10^{14}$	$5.6 \times 10^{15}$	$3.3 \times 10^{10}$
$n_i^{2+}$ ( $m^{-3}$ )	$5.1 \times 10^{15}$	$6.4 \times 10^{15}$	$3.1 \times 10^{15}$	$3.1 \times 10^{13}$	$2.1 \times 10^{15}$	$8.5 \times 10^9$
$n_i^{3+}$ ( $m^{-3}$ )	$1.1 \times 10^{13}$	$2 \times 10^{14}$	$3 \times 10^{14}$	$8.7 \times 10^{11}$	$3 \times 10^{14}$	$5.2 \times 10^8$
$\phi$ (V)	275.9	253.9	116.1	201.8	9.6	136.6
$j_{i\perp}^+$ ( $A/m^2$ )	14.1	2	7.5	$5.0 \times 10^{-2}$	3.0	$1.5 \times 10^{-5}$
$j_{i\perp}^{2+}$ ( $A/m^2$ )	1.9	1.5	4.2	$2.4 \times 10^{-2}$	3.1	$1.1 \times 10^{-5}$
$j_{i\perp}^{3+}$ ( $A/m^2$ )	$7.1 \times 10^{-3}$	$6.2 \times 10^{-2}$	0.8	$1.2 \times 10^{-3}$	1.0	$1.2 \times 10^{-6}$
$(K/q)_i^+$ (V)	13.7	15.5	100.9	12.8	74.2	54.5
$(K/q)_i^{2+}$ (V)	11.8	13.5	82.2	18.3	64.4	63.9
$(K/q)_i^{3+}$ (V)	16.6	15.1	65.8	34.9	57.0	73.4
$\Delta\phi$ (V)	26.5	43.1	35.0	37.4	46.5	44.4
$\theta^+$ (deg)	35.2	30.9	56.6	27.6	48.0	44.8
$\theta^{2+}$ (deg)	33.0	29	53.7	32.7	45.9	47.3
$\theta^{3+}$ (deg)	37.8	30.5	50.3	42.4	43.9	49.4
$Y^+$ ( $\times 10^{-2} mm^3/C$ )	0.7	1	3.7	0.8	2.9	2.3
$Y^{2+}$ ( $\times 10^{-2} mm^3/C$ )	0.7	0.9	3.1	1	2.6	2.6
$Y^{3+}$ ( $\times 10^{-2} mm^3/C$ )	0.9	1	2.6	1.7	2.4	2.9
$\varepsilon^+$ (mm/h)	$3.8 \times 10^{-4}$	$7.6 \times 10^{-5}$	$9.9 \times 10^{-4}$	$1 \times 10^{-6}$	$3.1 \times 10^{-4}$	$1.2 \times 10^{-9}$
$\varepsilon^{2+}$ (mm/h)	$4.6 \times 10^{-5}$	$5.2 \times 10^{-5}$	$4.8 \times 10^{-4}$	$8.9 \times 10^{-7}$	$2.9 \times 10^{-4}$	$1 \times 10^{-9}$
$\varepsilon^{3+}$ (mm/h)	$2.2 \times 10^{-7}$	$2 \times 10^{-6}$	$7.6 \times 10^{-5}$	$7.4 \times 10^{-8}$	$8.2 \times 10^{-5}$	$1.3 \times 10^{-10}$
<b>Total <math>\varepsilon</math> (mm/h)</b>	<b><math>4.3 \times 10^{-4}</math></b>	<b><math>1.3 \times 10^{-4} *</math></b>	<b><math>1.5 \times 10^{-3}</math></b>	<b><math>1 \times 10^{-6}</math></b>	<b><math>6.9 \times 10^{-4}</math></b>	<b><math>2.2 \times 10^{-9}</math></b>

\* This erosion rate is an overestimate of the real value in the BPT-4000 QLT because the numerical simulation geometry employs a sharp corner at this location whereas in the real geometry this corner was smoothed out by the erosion. The significance of this difference is that in the simulation the corner “interrupts” magnetic field streamlines leading to potential differences around the corner that allow ions to acquire kinetic energy. By contrast, the curvature of the eroded corner in the test follows closely the curvature of the streamline around that corner; the equipotentialization of the streamline reduces the acceleration of the ions around the corner and, in turn, the kinetic energy with which they impact the surface of the thruster.

## B. The basic physics of the erosion trends

Section IV-A quantified the erosion rates in the diverging section of the BPT-4000 acceleration channel and showed a significant reduction of the erosion in the steady-state geometry compared to the 1200-h geometry. In this section we discuss the basic physics that led to this reduction. We found that the process that led to the reduced erosion rates was in fact multifaceted. That is, several changes occurred in the plasma and magnetic field as the channel receded from its BOL geometry to its steady-state configuration that, when acting collectively, led to an effective shielding of the channel walls from ion bombardment. The changes in the plasma occurred as a consequence of the first-principles operational feature in these thrusters: the equipotentialization and isothermalization of the lines of force.<sup>19</sup>

The numerical simulations have shown that, with the exception of  $\theta$  whose impact was not found to be as critical, the remaining plasma properties pertinent to erosion were altered in the steady-state geometry in a manner that led to significant reductions of the erosion rate. Specifically, we found that the particular topology and magnitude of the magnetic field near the diverging walls<sup>††</sup> of this thruster in its steady-state configuration had the following consequences:

- 1) reduction of the accelerating electric field parallel to the wall, prohibiting ions from acquiring significant impact kinetic energy before entering the sheath,
- 2) reduction of the potential fall in the sheath along the wall, further diminishing the total impact energy that ions could gain before striking the material and,
- 3) reduction of the ion number density decreasing the flux of ions to the wall.

†† The magnetic field cannot be shown due to proprietary restrictions.

In support of these conclusions the reader is also referred to the contoured plots in Figure 14. The computed reductions for all ion species are provided in Tables 2 and 3. We also plot some of the tabulated results in Figure 18. We found the largest effects on the erosion to have been due to the lower total energy and flux of ions striking the wall. Regarding the effects of the incidence angle, we found them not to affect the erosion rate comparisons as significantly as the ion flux and impact energy. The bar plots for the incidence angle and erosion rates at the outer wall are provided in Figure 18 bottom-middle and bottom-right, respectively.

Regarding the effects of uncertainties in the plasma solution (as discussed in Section III-B), we note that the overall trend of the plasma potential inside the acceleration channel cannot be significantly different from the computed profile; Hall thrusters like the BPT-4000 all operate with the highest potential regions near the anode and the lowest potential regions in the exhaust. In the steady-state channel geometry of the BPT-4000, because the magnetic field streamline that “grazes” the diverging wall extends deep into the channel, it will be a line that is conclusively associated with high potentials. It is therefore marginally subject to the uncertainties of the plasma model. Because the fundamental principle that leads to the equipotentialization of the lines leads also to their isothermalization the arguments made about the plasma potential profile near the diverging section apply also to the electron temperature. Finally, it should be noted that the plasma density is likely much higher in the high-divergence regions of the channel and in the large-angle plume of the thruster than the values presently predicted by Hall2De, as suggested by the comparisons between theory and experiment in Section III-A, and the discussions of Section III-B. As also alluded to however by the discussion of Section III-B, the uncertainty of Hall2De’s plasma predictions is highest at the downstream point of the diverging walls and decreases as the upstream point is approached. A comparison of the erosion rates at location “D” (see Tables 2 and 3 and Figure 18) suggests a difference that exceeds 5 orders of magnitude. Thus, even if the true plasma density was higher by two orders of magnitude in the steady-state geometry than the value predicted by Hall2De, and if the density in the 1200-h geometry was not different, there would still be at least a three-order-of-magnitude reduction in the erosion rates at these locations of the walls.

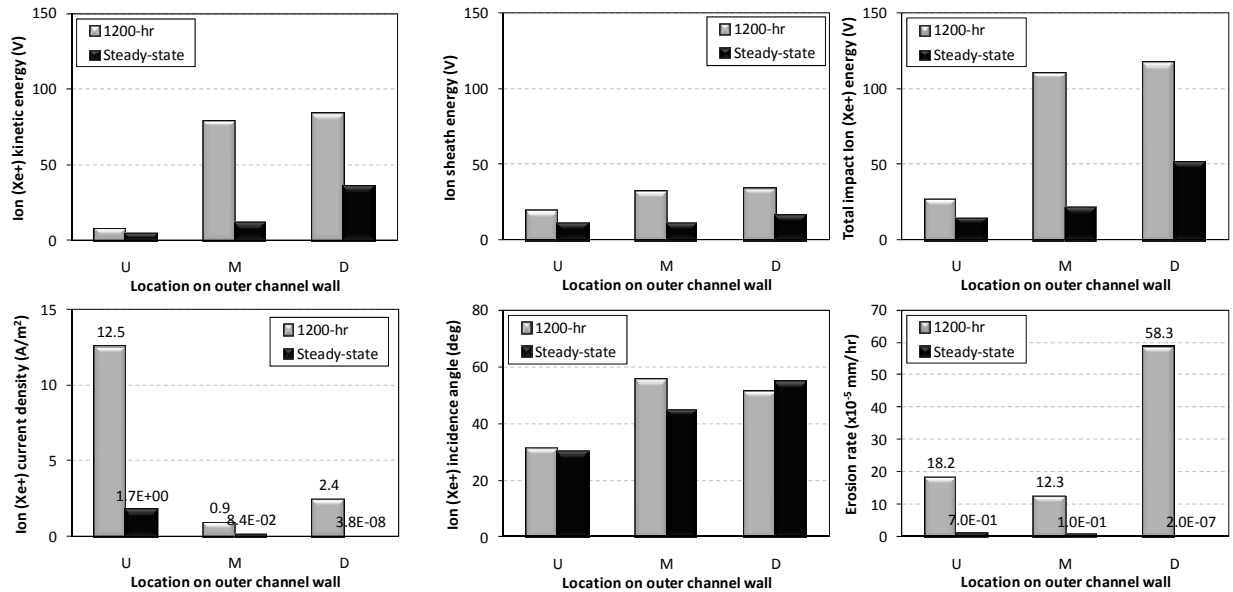


Figure 18. Bar plots of the erosion rates and relevant parameters at three locations on the outer wall of the BPT-4000 acceleration channel. The values shown here are for singly-charged ions only. Results for all ion charge states are shown in Tables 2 and 3 for the outer and inner walls, respectively.

## V. Conclusion

This paper provided possible explanations of the physics that led to the significantly-reduced erosion of the acceleration channel in Aerojet’s BPT-4000, a 4.5-kW Hall thruster that completed recently a >10,000-h QLT. The explanations have been based on 2-D axisymmetric simulations that were performed using the MFAM plasma solver Hall2De. Hall2De has been under development at JPL since 2009. The code’s main goal is to provide assessments of the life capability of existing Hall thruster systems and to guide the design of new long-life thrusters for NASA missions.

Several plasma and performance measurements were obtained in the BPT-4000 at JPL as part of a 2009 test campaign. The measurements have been used in this investigation to assess the fidelity of Hall2De. It is found that the agreement between simulation results and plasma measurements is within the experimental uncertainty for the majority of the comparisons we performed. In cases where the simulation results lie outside the experimental uncertainty we have identified the likely sources of discrepancy and assessed the impact of these discrepancies on our erosion predictions. We have found that the erosion rate reductions between the two simulated channel configurations - the 1200-h and the steady-state geometries - were different by many orders of magnitude at certain locations along the walls. Based on the wide range of comparisons performed with the plasma measurements, any improvements to our plasma model are not expected to yield differences between the two channel geometries that will exceed one order of magnitude. Thus, we conclude that the shielding of the channel surfaces was enabled by the specific topology of the magnetic field as illustrated by our plasma models.

The implications of magnetic shielding physics identified by Hall2De to exist in Aerojet's BPT-4000 Hall thruster design are potentially breakthrough. As our numerical simulations suggest, by properly shaping the magnetic field near the acceleration channel walls their erosion can be eliminated, thereby retiring the major perceived risk associated with the use of this electric propulsion technology onboard NASA science missions.

### Acknowledgments

The research described in this paper was carried out by the Jet Propulsion Laboratory, California Institute of Technology, under a contract with the National Aeronautics and Space Administration. Reference herein to any specific commercial product, process, or service by trade name, trademark, manufacturer, or otherwise, does not constitute or imply its endorsement by the United States Government or the Jet Propulsion Laboratory, California Institute of Technology.

### References

- <sup>1</sup> Oh, D. Y., "Evaluation of Solar Electric Propulsion Technologies for Discovery-Class Missions," *Journal of Spacecraft and Rockets*, 44, 2, 399-411 (2007).
- <sup>2</sup> Hofer, R. R., Randolph, T. M., Oh, D. Y., Snyder, J. S., and de Grys, K. H., "Evaluation of a 4.5 kW Commercial Hall Thruster System for NASA Science Missions," AIAA Paper 06-4469, July 2006.
- <sup>3</sup> Jacobson, D. T., Manzella, D. H., The United States of America as represented by the Administrator of the National Aeronautics and Space Administration, Washington, DC, U.S. Patent Application for "Elimination of Lifetime Limiting Mechanism of Hall Thrusters," Application No. 11/044,471, filed 28 Jan. 2005, Patent No. 7500350, issued 10 March 2009.
- <sup>4</sup> Kamhawi, H., Manzella, D., Mathers, A., and Aadland, R., "In-Space Propulsion High Voltage Hall Accelerator Thruster Development Project Overview," JANNAF Paper SPS-III-10 (Distribution A), December 2008.
- <sup>5</sup> Manzella, D., Oh, D., and Aadland, R., "Hall Thruster Technology for NASA Science Missions," AIAA Paper 05-3675, July 2005.
- <sup>6</sup> Kamhawi, H., Manzella, D., Pinero, L., Haag, T., Mathers, A., Liles, H., "In-Space Propulsion High Voltage Hall Accelerator Development Project Overview," AIAA Paper 09-5282, August 2009.
- <sup>7</sup> Kamhawi, H., Manzella, D., and Peterson, P., "High Voltage Hall Accelerator Wear Test Update," JANNAF Paper SPS-III-11, December 2008.
- <sup>8</sup> De Grys, K. H., Mathers, A., Welander, B., and Khayms, V., "Demonstration of >10,400 Hours of Operation on 4.5 kW Qualification Model Hall Thruster," AIAA Paper 10-6698, July 2010.
- <sup>9</sup> King, D. Q., de Grys, K. H., Aadland, R. S., Tilley, D. L., Voigt, A. W., "Magnetic Flux Shaping in Ion Accelerators with Closed Electron Drift," US Patent 6,208,080, 27 March 2001.
- <sup>10</sup> de Grys, K., et al., "4.5 kW Hall Thruster System Qualification Status," AIAA Paper 05-3682, July 2005.
- <sup>11</sup> Fife, J. M., "Hybrid-PIC Modeling and Electrostatic Probe Survey of Hall Thrusters," Ph.D. Thesis, Aeronautics and Astronautics, Massachusetts Institute of Technology, 1998.
- <sup>12</sup> Parra, F. I., Ahedo, E., Fife, J. M., and Martinez-Sanchez, M., "A Two-Dimensional Hybrid Model of the Hall Thruster Discharge," *Journal of Applied Physics*, 100, 023304 (2006).
- <sup>13</sup> Gamero-Castaño, M., and Katz, I., "Estimation of Hall Thruster Erosion Using HPHall," IEPC Paper 05-303, November 2005.
- <sup>14</sup> Hofer, R. R., Mikellides, I. G., Katz, I., and Goebel, D. M., "BPT-4000 Hall Thruster Discharge Chamber Erosion Model Comparison with Qualification Life Test Data," IEPC Paper 07-267, September 2007.

- <sup>15</sup> Hofer, R. R., Katz, I., Mikellides, I. G., Goebel, D. M., Jameson, K. K., Sullivan, R. M., and Johnson, L. K., "Efficacy of Electron Mobility Models in Hybrid-PIC Hall Thruster Simulations," AIAA Paper 08-4924, July 2008.
- <sup>16</sup> Mikellides, I. G., and Katz, I., Hofer, R. R., Goebel, D. M., "Hall-Effect Thruster Simulations with 2-D Electron Transport and Hydrodynamic Ions," IEPC Paper 09-114, September 2009.
- <sup>17</sup> Mikellides, I. G., Katz, I., Goebel, D. M., Jameson, K. K., and Polk, J. E., "Wear Mechanisms in Electron Sources for Ion Propulsion, II: Discharge Hollow Cathode," *Journal of Propulsion and Power*, 24, 4, pp. 866-879 (2008).
- <sup>18</sup> Mikellides, I. G., and Katz, I., "Wear Mechanisms in Electron Sources for Ion Propulsion, I: Neutralizer Hollow Cathode," *Journal of Propulsion and Power*, 24, 4, pp. 855-865 (2008).
- <sup>19</sup> Morozov A. I., and Savelyev, V. V., "Fundamentals of Stationary Plasma Thruster Theory," *Reviews of Plasma Physics*, 21, p. 203 (2000).
- <sup>20</sup> Marchand R., and Dumberry, M., "CARRE: A Quasi-Orthogonal Mesh Generator for 2D Edge Plasma Modeling," *Computer Physics Communications*, 96, pp. 232-246 (1996).
- <sup>21</sup> Lin, Z., Hahm, T. S., Lee, W. W., Tang, W. M., and White, R. B., "Turbulent Transport Reduction by Zonal Flows: Massively Parallel Simulations," *Science*, 281, pp. 1835-1837 (1998).
- <sup>22</sup> Dimits, A. M., "Fluid Simulations of Tokamak Turbulence in Quasiballooning Coordinates," *Physical Review E*, 48, pp. 4070-4079 (1993).
- <sup>23</sup> LeBrun, M. J., Tajima, T., Gray, M. G., Furnish, G., and Horton, W., "Toroidal Effects on Drift Wave Turbulence," *Physics of Fluids B*, 5, 3, pp. 752-773 (1993).
- <sup>24</sup> Marchand, R., Lu, J. Y., Kabin, K., and Rankin, R., "Unstructured Meshes and Finite Elements in Space Plasma Modelling: Principles and Applications," in *Advanced Methods for Space Simulations*, eds Usui, H. and Omura, Y., Terrapub, Tokyo, pp. 111-143 (2007).
- <sup>25</sup> Huang, W., Drenkow, B., and Gallimore, A. D., "Laser-Induced Fluorescence of Singly-Charged Xenon Inside a 6-kW Hall Thruster," AIAA Paper 09-5355, July 2009.
- <sup>26</sup> Müller, A. "Experimental Cross Sections for Electron-Impact Ionization and Electron-Ion Recombination," Research Coordination Meeting, IAEA CRP, Vienna, March 04-06, 2009 [http://www-dis.iaea.org/CRP/Heavy\\_elements/Presentations3/Mueller.pdf](http://www-dis.iaea.org/CRP/Heavy_elements/Presentations3/Mueller.pdf)
- <sup>27</sup> Bohm, D., Burhop, E., and Massey, H., *Characteristics of Electrical Discharges in Magnetic Fields*, ed. Guthrie, A. and Waterling, R. K., Eds., McGraw-Hill, New York, 1949.
- <sup>28</sup> Braginskii, S. I., "Transport Processes in Plasmas," *Reviews of Plasma Physics*, Vol. 1, ed. M. A. Leontovich, Consultants Bureau, New York, 1965, pp. 205-311.
- <sup>29</sup> Dugan, J. V. and Sovie, R. J., "Volume Ion Production Costs in Tenuous Plasmas: A General Atom Theory and Detailed Results for Helium, Argon and Cesium," NASA TN D-4150.
- <sup>30</sup> Mikellides, I. G., Katz, I., Goebel, D. M., and Polk, J. E., "Hollow cathode theory and experiment. II. A two-dimensional theoretical model of the emitter region," *Journal of Applied Physics*, 98, 113303 (2005).
- <sup>31</sup> Hobbs, G. D. and Wesson, J. A., "Heat Flow Through a Langmuir Sheath in the Presence of Electron Emission," *Plasma Physics*, 9, pp. 85-87 (1967).
- <sup>32</sup> Katz, I., and Mikellides, I. G., "A New Algorithm for the Neutral Gas in the Free-Molecule Regimes of Hall and Ion Thrusters," IEPC Paper 09-95, September 2009.
- <sup>33</sup> Katz, I., and Mikellides, I. G., "Neutral Gas Free Molecular Flow Algorithm Including Ionization and Walls for use in Plasma Simulations," submitted to the *Journal of Computational Physics* (2010), currently under review.
- <sup>34</sup> Hofer, R. R., Goebel, D. M., Snyder, J. S., Sandler, I. "BPT-4000 Hall Thruster Extended Power Throttling Range Characterization for NASA Science Missions," IEPC Paper 09-85, September 2009.
- <sup>35</sup> Hagelaar, G., Bareilles, J., Garrigues, L., and Boeuf, J. P., "Two Dimensional Model of a Stationary Plasma Thruster," *Journal of Applied Physics*, 91, p. 5592 (2002).
- <sup>36</sup> Bareilles, J., Hagelaar, G., Garrigues, L., Boniface, C., and Boeuf, J., "Critical Assessment of a Two-Dimensional Hybrid Hall Thruster Model: Comparisons with Experiments," *Physics of Plasmas*, 11, 6 (2004).
- <sup>37</sup> Barral, S., Makowski, K., Peradzynski, Z., Gascon, N., and Dudeck, M., "Wall Material Effects in Stationary Plasma Thrusters II: Near-Wall and in-Wall Conductivity," *Physics of Plasmas*, 10, 10, 4137-4152 (2003).
- <sup>38</sup> Raitses, Y., Staack, D., Keidar, M., and Fisch, N. J., "Electron-Wall Interaction in Hall Thrusters," *Physics of Plasmas*, 12, 057104 (2005).
- <sup>39</sup> Ahedo, E. and Parra, F. I., "Partial Trapping of Secondary-Electron Emission in a Hall Thruster Plasma," *Physics of Plasmas* 12, 073503 (2006).
- <sup>40</sup> Taccogna, F., Longo, S., and Capitelli, M., "Plasma Sheaths in Hall Discharge," *Physics of Plasmas*, 12, 093506 (2005).

- 
- <sup>41</sup> Ahedo, E., "Presheath/Sheath Model with Secondary Electron Emission from Two Parallel Walls," *Physics of Plasmas*, 9, 10, 4340-4347 (2002).
- <sup>42</sup> Katz, I., Hofer, R.R., Goebel, D.M., "Ion Current in Hall Thrusters," *IEEE Transactions on Plasma Science*, 36, 5, 1, pp. 2015-2023 (2008).
- <sup>43</sup> McDpnald, M. S., and Gallimore, A. D., "Cathode Position and Orientation Effects on Cathode Coupling in a 6-kW Hall Thruster," IEPC Paper 09-113, September 2009.
- <sup>44</sup> Hofer, R. R., Mikellides, I. G., Katz, I., and Goebel, D. M., "Wall Sheath and Electron Mobility Modeling in Hybrid-PIC Hall Thruster Simulations," AIAA Paper 07-5267, July 2007.
- <sup>45</sup> Yamamura, Y., and Tawara, H., "Energy Dependence of Ion-Induced Sputtering Yields from Monatomic Solids at Normal Incidence," *Atomic Data and Nuclear Data Tables* 62, 149-253 (1996).
- <sup>46</sup> Pencil, E. J., Randolph, T., and Manzella, D. H., "End-of-Life Stationary Plasma Thruster Far-Field Plume Characterization," AIAA Paper 96-2709, July 1996.